RESEARCH ARTICLE

Key Points:
- The Whole Atmosphere Community Climate Model has been extended to include ionospheric electrodynamics
- WACCM-X simulates the interaction of lower atmosphere and solar influences in the ionosphere
- Preliminary validation demonstrates agreement with observations

Correspondence to:
H.-L. Liu,
liuh@ucar.edu

Development and Validation of the Whole Atmosphere Community Climate Model With Thermosphere and Ionosphere Extension (WACCM-X 2.0)

Han-Li Liu[1] [ID], Charles G. Bardeen[2] [ID], Benjamin T. Foster[1], Peter Lauritzen[3] [ID], Jing Liu[1] [ID], Gang Lu[1] [ID], Daniel R. Marsh[1,2] [ID], Astrid Maute[1] [ID], Joseph M. McInerney[1] [ID], Nicholas M. Pedatella[1] [ID], Liying Qian[1] [ID], Arthur D. Richmond[1] [ID], Raymond G. Roble[1], Stanley C. Solomon[1] [ID], Francis M. Vitt[1,2] [ID], and Wenbin Wang[1] [ID]

[1]High Altitude Observatory, National Center for Atmospheric Research, Boulder, CO, USA, [2]Atmospheric Chemistry Observations and Modeling, National Center for Atmospheric Research, Boulder, CO, USA, [3]Climate and Global Dynamics, National Center for Atmospheric Research, Boulder, CO, USA

Abstract Key developments have been made to the NCAR Whole Atmosphere Community Climate Model with thermosphere and ionosphere extension (WACCM-X). Among them, the most important are the self-consistent solution of global electrodynamics, and transport of O^+ in the F-region. Other ionosphere developments include time-dependent solution of electron/ion temperatures, metastable O^+ chemistry, and high-cadence solar EUV capability. Additional developments of the thermospheric components are improvements to the momentum and energy equation solvers to account for variable mean molecular mass and specific heat, a new divergence damping scheme, and cooling by $O(^3P)$ fine structure. Simulations using this new version of WACCM-X (2.0) have been carried out for solar maximum and minimum conditions. Thermospheric composition, density, and temperatures are in general agreement with measurements and empirical models, including the equatorial mass density anomaly and the midnight density maximum. The amplitudes and seasonal variations of atmospheric tides in the mesosphere and lower thermosphere are in good agreement with observations. Although global mean thermospheric densities are comparable with observations of the annual variation, they lack a clear semiannual variation. In the ionosphere, the low-latitude E × B drifts agree well with observations in their magnitudes, local time dependence, seasonal, and solar activity variations. The prereversal enhancement in the equatorial region, which is associated with ionospheric irregularities, displays patterns of longitudinal and seasonal variation that are similar to observations. Ionospheric density from the model simulations reproduces the equatorial ionosphere anomaly structures and is in general agreement with observations. The model simulations also capture important ionospheric features during storms.

Plain Language Summary A comprehensive numerical model, the Whole Atmosphere Community Climate Model with thermosphere and ionosphere extension (WACCM-X), has been improved, in order to simulate the entire atmosphere and ionosphere, from the Earth's surface to ~700 km altitude. This new version (v. 2.0) adds the capability to calculate the motions and temperatures of ions and electrons in the ionosphere. The model results compare well with available ground-based and satellite observations, under both quiet and disturbed space weather conditions. Even with constant solar forcing, the model displays large day-to-day weather changes in the upper atmosphere and ionosphere, with basic patterns that agree with observations. This demonstrates the model ability to describe the connections between weather near the surface and weather in space.

1. Introduction

The terrestrial ionosphere exhibits variability on time scales ranging from minutes to diurnal, from days to solar rotations, and from solar cycles to centuries. These variations are primarily driven by manifestations of solar magnetism, including ultraviolet radiation, the solar wind, and the interplanetary magnetic field, which are processed by their interaction with the Earth's magnetosphere. Ionosphere density is a small fraction

(10^{-3} to 10^{-6}) of the neutral atmosphere density, and it has long been recognized that the thermospheric response to solar variation is important in determining ionospheric changes, since the neutral and ionized gases form a strongly coupled system that cannot be meaningfully described in isolation. The thermosphere and ionosphere are integral parts of the whole atmosphere system, and more recent perspectives emphasize the importance of lower atmospheric dynamics and chemistry, including weather systems, gravity waves, planetary waves, tidal variations, seasonal cycles, and long-term climate change, in driving the variability of thermosphere-ionosphere system (e.g., Goncharenko et al., 2010a, 2010b; Immel et al., 2006; Liu, 2016; Liu & Roble, 2002; Pedatella et al., 2012; Qian et al., 2009; Solomon et al., 2015b).

Numerical modeling of the thermosphere-ionosphere system has historically been approached by specifying upper boundary conditions representing solar and magnetospheric processes, and lower boundary conditions representing climatological or parameterized forcing of atmospheric state variables at some interface, generally in the stratosphere-mesosphere region. For instance, the NCAR Thermosphere-Ionosphere-Electrodynamics General Circulation Model (TIE-GCM; Qian et al., 2014; Richmond et al., 1992) and Thermosphere-Ionosphere-Mesosphere-Electrodynamics General Circulation Model (TIME-GCM; Roble & Ridley, 1994) have lower boundaries at 97 and 30 km, respectively; these lower boundary conditions are specified using tidal parameterizations or observed meteorological fields (e.g., Hagan et al., 2007). However, with the development of Whole Atmosphere Models (e.g., Akmaev, 2011; Marsh et al., 2007), there is an opportunity to adopt a fully self-consistent numerical description of the entire atmosphere-ionosphere system. Early efforts to accomplish this are described in Liu et al. (2010). In this paper, we describe new advances of the NCAR WACCM-X that now forms a comprehensive description of atmosphere-ionosphere interaction. The most important of these are the incorporation of a fully coupled low and middle latitude electrodynamo, dynamical transport of the atomic oxygen ions, and high-latitude forcing by the magnetospheric electric fields and auroral Joule and particle heating.

2. Thermosphere-Ionosphere Extension of the Whole Atmosphere Community Climate Model

WACCM-X is a configuration of the NCAR Community Earth System Model (CESM; Hurrell et al., 2013) that extends the atmospheric component into the thermosphere, with a model top boundary between 500 and 700 km. As a part of CESM, WACCM-X is uniquely capable of being run in a configuration where the atmosphere is coupled to active or prescribed ocean, sea ice, and land components, enabling studies of thermospheric and ionospheric weather and climate. Physical processes represented in WACCM-X build upon those in regular WACCM, which has a model top at ~130 km, and in turn is built upon the Community Atmosphere Model (CAM), which goes up to ~40 km. The physics of these models is described in Marsh et al. (2013) and Neale et al. (2013). Recent revisons and improvements to WACCM, which are therefore included in WACCM-X, include the following:

1. Revision of parameterized nonorographic gravity wave forcing as described by Richter et al. (2010) and Garcia et al. (2017).
2. Introduction of surface stress due to unresolved topography that led to significant improvements in the frequency of stratospheric sudden warmings (Marsh et al., 2013; Richter et al., 2010).
3. Chemical kinetic and photochemical rate constants updated to the Jet Propulsion Laboratory recommendations (Sander et al., 2011).
4. A new treatment of stratospheric heterogeneous ozone loss (Solomon et al., 2015a).
5. Protocols from the Chemistry Climate Model Initiative (Eyring et al., 2013) are used for the specification of time-dependent greenhouse gases and ozone depleting substances.

In addition, two metastable O^+ states, $O^+(^2D)$ and $O^+(^2P)$, have been added to the chemistry package, which already includes 5 ions (O^+, O_2^+, NO^+, N^+, and N_2^+), electrons, and 74 neutral species. The model has 87 photolysis and photoionization reactions and 202 gas phase and heterogeneous reactions. The specification of solar spectral irradiance at wavelengths from Lyman-α to the near infrared are unchanged from Marsh et al. (2013) and continues to use the empirical model of Lean et al. (2005). EUV and X-ray fluxes implemented are described below.

At the standard model resolution, the model does not generate a quasi-biennial oscillation, but one can be imposed by relaxing the equatorial zonal winds in the stratosphere to the observed QBO zonal winds.

Alternatively, for simulations of particular years in the recent historical record, WACCM-X has the option to constrain the tropospheric and stratospheric dynamics by reanalysis, namely, the "specified-dynamics" or SD version of the model. This is currently done by relaxing temperature, zonal, and meridional winds up to ~50 km and surface pressure toward the Modern Era Retrospective Analysis for Research and Applications (MERRA; Rienecker et al., 2011).

WACCM-X is currently based on CAM-4 physics, as released in CESM 1.0, and employs a conventional latitude-longitude grid with horizontal resolution of 1.9° in latitude and 2.5° in longitude. Thus, it lags the incipient release of CESM 2.0, in which CAM and WACCM can be run at twice that resolution. The default vertical resolution is the same as WACCM below 0.96 hPa but has been increased to one-quarter scale height above that pressure level. The model top pressure (p) is 4.1×10^{-10} hPa (typically between 500 and 700 km, depending on the solar and geomagnetic activity). Note that it is common practice to refer to log-pressure level as Z_p in units of scale height relative to a reference pressure, as is done in the TIE-GCM. The WACCM-X model top is equivalent to $Z_p = 7.1$, where $Z_p = \ln(p_0/p)$ and $p_0 = 5 \times 10^{-7}$ hPa. It is about 28.5 scale heights above the Earth surface. A constant gravity acceleration (g), with the value at the Earth surface, is currently used in the model. It is thus necessary to rescale the model geopotential height, which is based on the constant g, according to gravitational law when analyzing model output. The model grid system does not consider the size differential of the upper and lower sides of grid cells, which may introduce errors on the order of z/r_e (z is the altitude and r_e is the Earth radius) for vertical flux quantities.

Earlier work, and the initial release of WACCM-X 1.0 (Liu et al., 2010), included diffusive processes in the neutral thermosphere and a preliminary implementation of thermospheric neutral dynamics, using the CAM dynamical core, but did not include neutral wind dynamo, ionospheric transport, or calculation of ion/electron energetics and temperatures. WACCM-X 1.0, therefore, does not correctly resolve the thermospheric energetics or thermal structure. These processes, as well as many additional processes included in models such as the TIE-GCM have now been implemented in the new model. Compared with TIE-GCM and TIME-GCM, WACCM-X 2.0 has the advantage of self-consistently resolving lower atmospheric processes and therefore enables more realistic simulation of upper atmospheric variability due to lower atmospheric forcing and better understanding and quantification of space weather and space climate. The model will be released as WACCM-X 2.0, and the following is a detailed description of the new developments.

2.1. Neutral Thermosphere Components

Although in the early version of WACCM-X species dependent specific heats and mean molecular weight (and along with it the gas constant of dry air) were taken into account in the physics modules (Liu et al., 2010), these quantities were treated as constants in the finite volume (FV) dynamical core (often referred to as dycore). Changes have been made in the FV dycore to treat them properly (sections 2.1.1 and 2.1.3). Changes in divergence damping are described in section 2.1.2. Cooling of the neutral atmosphere by O(^{3}P) fine structure emission is now included in the model, as described in section 2.1.4.

2.1.1. Momentum Equations

In the standard FV dycore, the vertical coordinate is based on Exner function p^κ (where κ is the ratio of gas constant of dry air R and specific heat at constant pressure c_p). Accordingly the pressure gradient calculation, using the contour integral method (Lin, 1997), uses the Exner function. When κ is a constant (below the homopause), a constant pressure surface translates to a surface with a constant Exner function, and the pressure gradient calculation is valid. However, this is no longer true when κ becomes a variable above the homopause: the control volume is distorted and the pressure gradient calculation is incorrect. This leads to excessively large mean meridional and vertical winds, and erroneous temperature structures in the thermosphere. This problem is solved by changing from Exner function based vertical coordinate to log-pressure vertical coordinate.

2.1.2. Divergence Damping

The FV discretization is designed to damp vorticity at grid scale (Lin & Rood, 1996, 1997), but an explicit scheme is needed to damp divergence and avoid spurious accumulation of the divergent component of total kinetic energy. In earlier versions of CAM, WACCM and WACCM-X, the second-order divergence damping was the default, with a damping coefficient, $r_e^2 \Delta\lambda \Delta\theta / 128\Delta t$ (where $\Delta\lambda, \Delta\theta$, and Δt are longitude and latitude spacing, and time step, respectively), applied uniformly at all grid points, except at the top three levels, where it monotonically increases by about fourfold. In our numerical experiments using WACCM-X, however, we found that the second-order divergence damping with the default damping coefficient is

responsible for damping atmospheric tidal waves. By reducing the damping coefficient, the tidal amplitudes become much stronger than previously reported (Liu et al., 2010) and are comparable with observations. In more recent versions of the FV dycore, a fourth-order divergence damping has been introduced (Lauritzen et al., 2012). It has the advantage of more selectively damping out small-scale waves, while minimally impact planetary-scale waves. This is now the default option for WACCM-X.

2.1.3. Energy Equation and Hydrostatic Equation

The formulation of the energy equation of the neutral atmosphere in the standard FV dycore is based on potential temperature (Θ). Potential temperature, however, is not a well defined quantity in the thermosphere, where the mixing ratios of the major species are variables: when adiabatically moved to a reference level, the composition of an air parcel is likely to be different from that of the reference level atmosphere. This problem can be avoided if the energy equation is formulated based on temperature. It is also possible to work with the current FV formulation, by taking into account the κ variability when solving for potential temperature:

$$\frac{\partial \Theta \delta p}{\partial t} + \nabla_H \cdot (\mathbf{V_H} \Theta \delta p) = \Theta \ln (p/p_0) \left(\frac{\partial \kappa \delta p}{\partial t} + \nabla_H \cdot (\mathbf{V_H} \kappa \delta p) \right) \tag{1}$$

where δp is the layer thickness, ∇_H the horizontal divergence, and $\mathbf{V_H}$ is the horizontal wind vector. It is noted that the correction term on the right-hand side of equation (1) is actually in the form of the advection of κ. Therefore, it is convenient to implement this correction term by treating κ as a tracer species. It is found that without this correction, spurious waves could be excited that become very large in the upper thermosphere, ultimately rendering the model unstable.

In the FV dycore, the following form of the hydrostatic equation, also based on potential temperature, is used to calculate geopotential Φ_{gp}: $\delta \Phi_{gp} = c_p \Theta \delta (p^\kappa)$. This relationship is incorrect with κ being a variable. The correct form

$$\delta \Phi_{gp} = c_p \kappa p^\kappa \Theta \delta(\ln (p)) \tag{2}$$

is used instead.

2.1.4. Cooling by O(^{3}P) Fine Structure Emission

The primary radiative cooling mechanisms for the thermosphere are excitation of CO_2 and NO by collisions with atomic oxygen, followed by infrared emission. These were included in the first version of WACCM-X. However, in the upper thermosphere, fine structure emission by O(^{3}P) at 63 μm is also important. This is calculated based on the local thermodynamic equilibrium (LTE) expression in Bates (1951) for the O(^{3}P) cooling rate $L_{O(^3P)}$ in erg g^{-1} s^{-1}:

$$L_{O(^3P)} = 0.835 \times 10^{-18} \frac{n([O])}{\rho} X_{fac} \frac{\exp (-228/T)}{1 + 0.6 \ \exp (-228/T) + 0.2 \ \exp (-325/T)} \tag{3}$$

where $n([O])$ is the atomic oxygen number density (in cm^{-3}), ρ is the total mass density (in g cm^{-3}), and T is the neutral temperature (in Kelvin). X_{fac} is a masking factor for radiative transfer in an optically thick medium, based on Kockarts and Peetermans (1970). This mechanism is included in WACCM-X 2.0, providing about -50 K temperature reduction at high altitudes, thus offsetting to some extent the additional heating generated by inclusion of O$^+$ metastables (see below).

2.2. Ionospheric Components

The new ionospheric component in WACCM-X includes modules of the ionospheric wind dynamo, F-region O$^+$ transport, and electron and ion temperatures, which are used to calculate heating of the neutral atmosphere through collisions with thermal electrons and ions. Also, two metastable O$^+$ states, O$^+$(^{2}D) and O$^+$(^{2}P), have been added to the WACCM-X chemistry package.

2.2.1. Electrodynamics

The ionospheric electrodynamics in WACCM-X are adapted from the TIE-GCM with the general aspects of modeling ionospheric electrodynamics discussed in Richmond and Maute (2014) and the specific details about TIE-GCM 2.0 electrodynamics given in Maute (2017). In the following, we describe in general terms the WACCM-X electrodynamics and point out differences with respect to the TIE-GCM electrodynamics.

In the thermosphere, ion-neutral coupling becomes important, and, through ion drag, neutral dynamics are influenced by the plasma motion and its associated electric field. Ion drag calculation is already included in

WACCM-X 1.0, but the ion drifts are specified empirically. WACCM-X 2.0 electrodynamics calculate self-consistently electric fields and thus ion drifts at low and middle latitude, driven by the neutral wind dynamo. At high latitudes, the electric potential is imposed by an empirical model. Smaller forcing terms due to gravity and plasma pressure gradient driven current are neglected. Ionospheric electrodynamics in WACCM-X are treated as steady state, with an electrostatic electric field E expressed by an electrostatic potential Φ through $E = -\nabla\Phi$. The ionospheric conductivities are highly anisotropic, with conductivities along the geomagnetic field lines several orders of magnitude larger than those perpendicular to the geomagnetic field. Therefore, on the spatial and temporal scales considered in WACCM-X, the geomagnetic field lines at middle and low latitude are considered equipotential at conjugate points.

The electrodynamics are formulated in a modified magnetic apex coordinate system (Richmond, 1995) using a realistic geomagnetic main field which is updated once per year based on the International Geomagnetic Reference Field (IGRF; Thébault et al., 2015). The resulting partial differential equation is solved for the electric potential Φ given by Richmond (1995, equation (5.23)) using the field line integrated quantities in Richmond (1995, equations (5.11)–(5.29)). The ionospheric conductivities below ∼80 km are assumed to be negligible, so the bottom boundary of the field line integration is set to a pressure level of 1.0 Pa, which is equivalent to ∼80 km. The reference height at which the electric potential is determined is also set to 80 km. The spatial resolution of the ionospheric electrodynamics in WACCM-X is the same as in the TIE-GCM, 4.5° in magnetic longitude, and varying from 0.34° to 3.07° in magnetic latitude from the equator to the poles. Coordinate transform routines from the Earth System Modeling Framework (ESMF) are employed for mapping between the geographic and geomagnetic coordinate systems.

The electrodynamics solver obtains the global electric potential due to the wind dynamo at low and middle latitudes, with a high-latitude boundary condition prescribed by empirical electric potential patterns to simulate magnetospheric forcing. In the current version of WACCM-X, the empirical ion convection patterns are from Heelis et al. (1982) (see section 2.2.5). The wind dynamo is merged with the high latitude prescribed electric potential between 60° and 75° magnetic latitude, which allows the high-latitude potential to influence the low-latitude electrodynamo, approximating the effect of a penetration electric field.

2.2.2. O$^+$ Transport

Ion transport in WACCM-X 2.0 is calculated using the approximation that O$^+$ in the (^{4}S) ground state is the only ion that has a long enough lifetime to be subject to significant transport. Molecular ions have lifetimes that are short compared to the chemistry time step of 5 min (except in the lower E-region, where transport is a minor consideration, and below 200 km at night, when the ion densities are so low they have little influence on the thermosphere). The light atomic ions H$^+$ and He$^+$, and metallic ions, are not yet included in the model. The excited metastable states of O$^+$ (see below) also have short lifetimes, and N$^+$ is considered a sufficiently minor species that any F-region transport will remain in chemical equilibrium with O$^+$.

The basic method is that O$^+$ transport is calculated separately from chemical production and loss (which is part of the interactive chemistry module), and the electron density is then adjusted to preserve charge neutrality. The dynamical solution is adapted from the TIE-GCM method described by Roble et al. (1988), and is summarized as follows.

The equation

$$\frac{\partial n_i}{\partial t} = -\nabla \cdot (n_i \mathbf{V_i}) \tag{4}$$

describes the transport of O$^+$, in terms of its number density n_i, by field-aligned plasma ambipolar diffusion, $E \times B$ drifts perpendicular to the magnetic field lines, and neutral winds along the magnetic field lines, where ion velocity $\mathbf{V_i}$ is defined as

$$\mathbf{V_i} = \mathbf{V_\parallel} + \mathbf{V_\perp} \tag{5a}$$

$$\mathbf{V_\parallel} = (\mathbf{b} \cdot \frac{1}{v_{in}}[\mathbf{g} - \frac{1}{\rho_i}\nabla(P_i + P_e)] + \mathbf{b} \cdot \mathbf{V})\mathbf{b} \tag{5b}$$

$$\mathbf{V_\perp} = \frac{\mathbf{E} \times \mathbf{B}}{|B|^2} \tag{5c}$$

where $\mathbf{V_\parallel}$ and $\mathbf{V_\perp}$ are the parallel and perpendicular ion velocities with respect to the geomagnetic field lines. The unit vector along the geomagnetic field line is $\mathbf{b}$, v_{in} is the O$^+$ ion-neutral collision frequency, $\mathbf{g}$ is

gravity, ρ_i is the O^+ mass density, P_i and P_e are the ion (O^+) and electron pressure, **V** is the neutral wind velocity, $|B|$ is the geomagnetic field strength, and **E** is the electric field. Note that equation (5c) neglects the influence of ion-neutral collisions on ion motion perpendicular to **B**; this influence is significant only in the E-region where the O^+ lifetime is short and transport is unimportant.

Equation (4) is solved on the WACCM-X geographic latitude/longitude grid and pressure levels, using the finite difference method (Roble et al., 1988; Wang, 1998). The time integration is explicit in the horizontal direction and implicit in the vertical direction.

The lower boundary condition is specified by assuming chemical equilibrium between ion species. The top boundary condition is given in terms of the ambipolar diffusive flux of O^+:

$$-b_z^2 D_A \left(2T_p \frac{\partial}{\partial z} + \frac{m_i g}{R^*} \right) n_i = \Phi_i \tag{6}$$

where D_A is the ambipolar diffusion coefficient, $T_p = (T_i + T_e)/2$ is plasma temperature, R^* is the universal gas constant, m_i is the mass of O^+, and b_z is the vertical component of the magnetic field. Φ_i is the ambipolar diffusion flux of O^+ at the top boundary, describing the O^+ transport to and from the plasmasphere. It is usually upward (positive) during the day and downward at night (negative). In the model, it depends on magnetic latitude and solar local time, and its maximum magnitudes for day and night can be specified separately ($\pm 2 \times 10^8$ cm^{-2} s^{-1} is currently used for day and night, respectively). A detailed description of this dependence can be found in Wang (1998).

2.2.3. Metastable O^+ Chemistry and Energetics

The ion chemistry in WACCM-X 1.0 was modified to include ionization of the excited metastable ion species $O^+(^2D)$ and $O^+(^2P)$ and their loss reactions. These have a small effect on E-region chemistry, but are significant in the F-region because they provide more rapid paths for transfer of ionization to molecules and their subsequent neutralization through dissociative recombination, thus reducing total plasma density. These reactions also contribute to chemical heating through their exothermicity, so including them raises the neutral temperature of the upper thermosphere by about 50–100 K. Earlier model versions that did not include the metastable ions put all of the ionization into $O^+(^4S)$, thereby neglecting the additional solar energy that goes into the excited states, and ultimately into the neutral heating rate. Ionization/excitation rates are included in the solar parameterization described in the next section, and chemical reaction rates are adopted from Roble (1995).

2.2.4. Solar EUV Ionization and Heating

The solar extreme-ultraviolet (EUV) variability and energy deposition scheme, including photoelectron effects, is described in Solomon and Qian (2005), and is essentially unchanged from earlier versions of WACCM and WACCM-X, except for a correction to the molecular oxygen cross section in the 105–121 nm band as described by Garcia et al. (2014). However, an optional file-based input now provides a means for running the model with any solar spectral input. This includes solar flare simulation capability, with solar spectra input at a 5 min cadence to match the physics/chemistry time step. Solar spectra can be from either high-time-resolution models, or measurements. Solar spectra estimated by the Flare Irradiance Spectral Model (FISM; Chamberlin et al., 2007, 2008) are used as the default solar flare spectra input in the current version (cf., Qian et al., 2010).

At night, the lower ionosphere does not entirely disappear, due to some EUV photons multiply-scattered by the exosphere reaching the nightside of the Earth. Starlight may also contribute to night time ionization, but this is currently neglected in WACCM-X. A simplified estimation of this background ionization is applied equally to all model columns, including on the dayside. For consistency, the method used in the TIE-GCM, the TIME-GCM, and the Global Airglow model, is adapted (Solomon, 2017). This considers the primary sources of night ionization to be geocoronal emissions by hydrogen (H Lyman-α at 121.6 nm and H Lyman-β at 102.6 nm) and helium (He I at 58.4 nm and He II at 30.4 nm). These are absorbed using a nominal cross section for each line, and distributed through the column using Beer's law, imagining an overhead, invariant flux. This is a gross approximation to the actual geocoronal illumination, but results in reasonable comparison with observations of the nightside ionosphere, with ion density around 10^3 cm^{-3} in the E-region ($\sim$100–150 km) and 10^2 cm^{-3} in the D region ($\sim$80–100 km). A more sophisticated parameterization, for future consideration, is provided by Titheridge (2003).

2.2.5. High-Latitude Ionospheric Inputs

At high latitudes, the effects of the magnetospheric current system are applied using an electric potential pattern and an auroral precipitation oval. The Heelis et al. (1982) empirical specification of potential,

parameterized by the geomagnetic Kp index as described by Emery et al. (2012), is employed, and ionization from auroral precipitation is specified using the formulation described by Roble and Ridley (1987), based on the estimated hemispheric power of precipitating electrons. The empirical estimate of this power as it depends on Kp has been increased from the original formulation by an approximate factor of two for high Kp, based on results obtained by Zhang and Paxton (2008) from the Global Ultraviolet Imager (GUVI) on the TIMED satellite. These results give a hemispheric power of, for example, ∼40 GW at Kp = 3, increasing to ∼150 GW at Kp = 7 (Solomon et al., 2012).

2.2.6. Electron and Ion Temperature

A complete treatment of electron temperature would consider the adiabatic expansion, heat advection, electron heat flux due to electric current and thermal conduction, heating associated with production of electron-ion pairs due to photochemical and auroral processes, and cooling due to collisions with neutral and ion species. In the terrestrial ionosphere, however, adiabatic expansion and heat advection are negligible. Furthermore, with the assumptions that the electron heat flux being along the magnetic field lines and the field-aligned currents not present, and the dominant temperature gradients being in the vertical, only thermal conduction in the vertical direction is considered for the ionosphere (e.g., Rees & Roble, 1975; Schunk & Nagy, 2009)

$$\frac{3}{2}n_e k \frac{\partial T_e}{\partial t} = \sin^2 I \frac{\partial}{\partial z}\left(\mu_e \frac{\partial T_e}{\partial z}\right) + \sum Q_e - \sum L_e \tag{7}$$

where n_e and T_e are electron number density and electron temperature, respectively, μ_e the electron thermal conductivity, $\sum Q_e$ and $\sum L_e$ are total heating and cooling rates, respectively, and I is the geomagnetic dip angle. Calculation of μ_e follows the formulation given by Rees and Roble (1975) (also used in TIE-GCM). The total heating rate is proportional to the production rates of electron-ion pairs from all photochemical reactions (including those involving metastable O^+ states) and auroral processes. The heating efficiency uses the empirical formulation by Swartz and Nisbet (1972) and will be updated to the new formulation of Smithtro and Solomon (2008). The cooling rates include electron energy loss through collisions with ions and neutrals, and the formulations follow that of Rees and Roble (1975) (again the same as those used in TIE-GCM). The energy loss to the neutrals is then used to calculate the heating of neutrals by thermal electrons.

Equation (7) could be further simplified by making a quasi steady state assumption, which is the approach taken in the TIE-GCM formulation. However, a numerical study by Roble and Hastings (1977) found that between 300 and 600 km altitude, it would take 200–1,000 s to reach steady state. With the usual time step of 300 s in WACCM-X, the steady state assumption may not be valid. Therefore, a time-dependent equation (7) is solved in WACCM-X, using the Crank-Nicolson method. Because the equation is highly nonlinear, the solver is applied iteratively to obtain convergence.

The following empirical topside heat flux has been used at the upper boundary in the TIE-GCM and is adapted here:

$$F_{top}^e = \begin{cases} F_{top}^{eD} & \text{if } \zeta \leq 80° \\ (F_{top}^{eD}+F_{top}^{eN})/2+(F_{top}^{eD}-F_{top}^{eN})/2\cos\left(\frac{\zeta-80°}{20°}\pi\right) & \text{if } 80° < \zeta < 100° \\ F_{top}^{eN} & \text{if } \zeta \geq 100° \end{cases} \tag{8}$$

where ζ is solar zenith angle, and the daytime and nighttime heating flux F_{top}^{eD} and F_{top}^{eN} are defined as

$$F_{top}^{eD} = \begin{cases} -2.25\times10^7 F10.7(1+\sin\left(\frac{|\phi_M|-30°}{60°}\pi\right))/2 & \text{if } |\phi_M| < 60° \\ -2.25\times10^7 F10.7 & \text{if } |\phi_M| \geq 60° \end{cases} \tag{9}$$

$$F_{top}^{eN} = F_{top}^{eD}/5 \tag{10}$$

where ϕ_M is the geomagnetic latitude, and F10.7 is the solar 10.7 cm radio flux with solar flux unit (sfu, 1 sfu = 10^{-22} W m^{-2} Hz^{-1}). The unit of the heat flux is eV cm^{-2} s^{-1}.
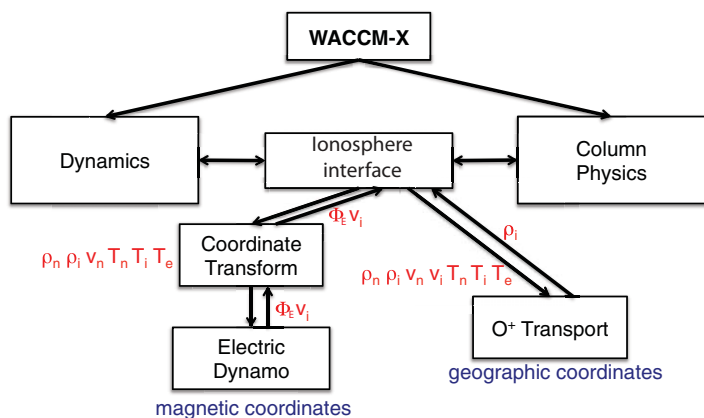
Figure 1. Schematic diagram describing the coupling of the ionospheric modules with other model components through ionosphere_interface module. ρ, $\mathbf{v}$, and T are density, velocity, and temperature, respectively, with subscript n, i, and e denoting neutral, ion, and electron, respectively. Φ_E is electric potential.

The ion temperature T_i is calculated by assuming equilibrium between the heating of the ions by electron-ion Coulomb interactions, Joule heating and the cooling through ion-neutral collisions (e.g., Schunk & Nagy, 2009).

2.3. Model Structure and Configuration

The ionospheric wind dynamo and O^+ transport in the F-region are solved using geomagnetic coordinates and geographic coordinates, respectively, as discussed in previous sections. WACCM-X ionosphere modules are coupled to the physics decomposition via an interface layer (ionosphere_interface). The ionosphere interface layer implemented uses the FV dynamics-physics (DP) coupling methodology, which has access to physical quantities in geographic coordinates, and also provides the infrastructure to distribute the output of the ionospheric modules, along with updates from dynamical core calculations, to the column physics decomposition. Figure 1 is a schematic diagram showing how the ionosphere_interface module interacts with other model components. As noted above, ESMF parallel mapping routines are used to transform fields between the geographic and geomagnetic grids. Other ionosphere models will need to provide an ionosphere_interface module that could be modeled after WACCM-X's interface module.

A 5 min time step is used for advancing tendencies in column physics, while subcycling is used for dynamics and species transport due to large wind velocities, especially in the thermosphere (the default subcycling is eight dynamical time steps per every physics time step). The time step and the subcycling number can be adjusted as needed. By comparison, CAM and regular WACCM generally use a 30 min physics time step. Since WACCM-X has more altitude levels and performs additional ionospheric calculations, it is therefore a relatively computationally intensive model. However, it scales reasonably well in the current parallel implementation, for example, one model-year runs in 0.75 days of wall-clock time on 864 cores (24 nodes on the NCAR supercomputer "cheyenne"), which is a model-time to real-time ratio of almost 500.

3. Evaluation and Validation of Model Results

Several sets of WACCM-X simulations have been conducted and used for model evaluation and validation: (i) Solar maximum simulation (one model-year), with F10.7 set at a constant 200 sfu. The Kp index is set to a constant low value (0.3). Apart from being a baseline test of the model, the simulation with constant solar and geomagnetic conditions is used to evaluate the impact of lower atmosphere forcing on the variability of the thermosphere and ionosphere. (ii) Solar minimum simulation, using daily F10.7 and Kp values for the year of 2008. (iii) Simulations using daily F10.7 and Kp values for September–December 2002 and June–July 2007. (iv) Simulation using daily F10.7 and 3-hourly Kp values covering March 2013. All four sets are free-run simulations (without constraining the lower atmosphere with reanalysis data). Table 1 is a summary of main setting of these simulations.

In the following, simulations in (i) and (ii) are used to evaluate general features of the thermosphere and ionosphere under solar maximum and minimum conditions, respectively, while the simulations in (iii) are used for direct comparison with GUVI measurements and the NRLMSIS empirical model results (Picone

Table 1
WACCM-X Simulations Used for This Study

|	F10.7 (sfu)	Kp	Simulation time
i	200	0.3	January–December
ii	Daily	Daily	January 2008 to February 2009
iii	Daily	Daily	September–December 2002 and June–July 2007
iv	Daily	3-Hourly	March 2013

*Note.* All are free-run simulations.

et al., 2002) under different solar conditions. Simulation in (iv) is used to study ionospheric responses to the geomagnetic storm on 17 March 2013.

3.1. Thermal and Compositional Structures

A known problem in the previous version of WACCM-X is that the thermosphere was on average 100–200 K too cold compared with climatology. This was mainly due to the absence of thermal electron heating in the model, which is an important heat source in the upper thermosphere (e.g., Roble, 1995). As discussed in the previous section, thermal electron heating is now included. The global mean electron and ion temperatures from the model are shown in Figures 2a and 2c, for solar maximum and solar minimum conditions, respectively. These values are in good agreement with previous model results from the TIE-GCM and TIME-GCM, although the electron temperatures are generally hotter at high altitude than standard climatologies, e.g., the International Reference Ionosphere (Bilitza, 2001). Since the ionospheric electron temperature is usually inversely proportional to the electron density, a possible cause of the hotter electron temperature is that the model electron density is systematically lower than observations (section 3.3.2; J. Liu et al., First results from ionospheric extension of WACCM-X during the deep solar minimum year 2008, submitted to *Journal of Geophysical Research: Space Physics*, 2017). Global mean neutral temperature is also shown in Figures 2a and 2c. The upper thermosphere temperature is much warmer than earlier results: the global mean temperature is ~1,240 K under solar maximum conditions and ~700K under solar minimum conditions, while these values were ~960 K and ~565 K, respectively, for the same solar conditions in the earlier version of the model. The latitude and altitude structures of the zonal mean temperature are shown in Figures 2b and 2d.
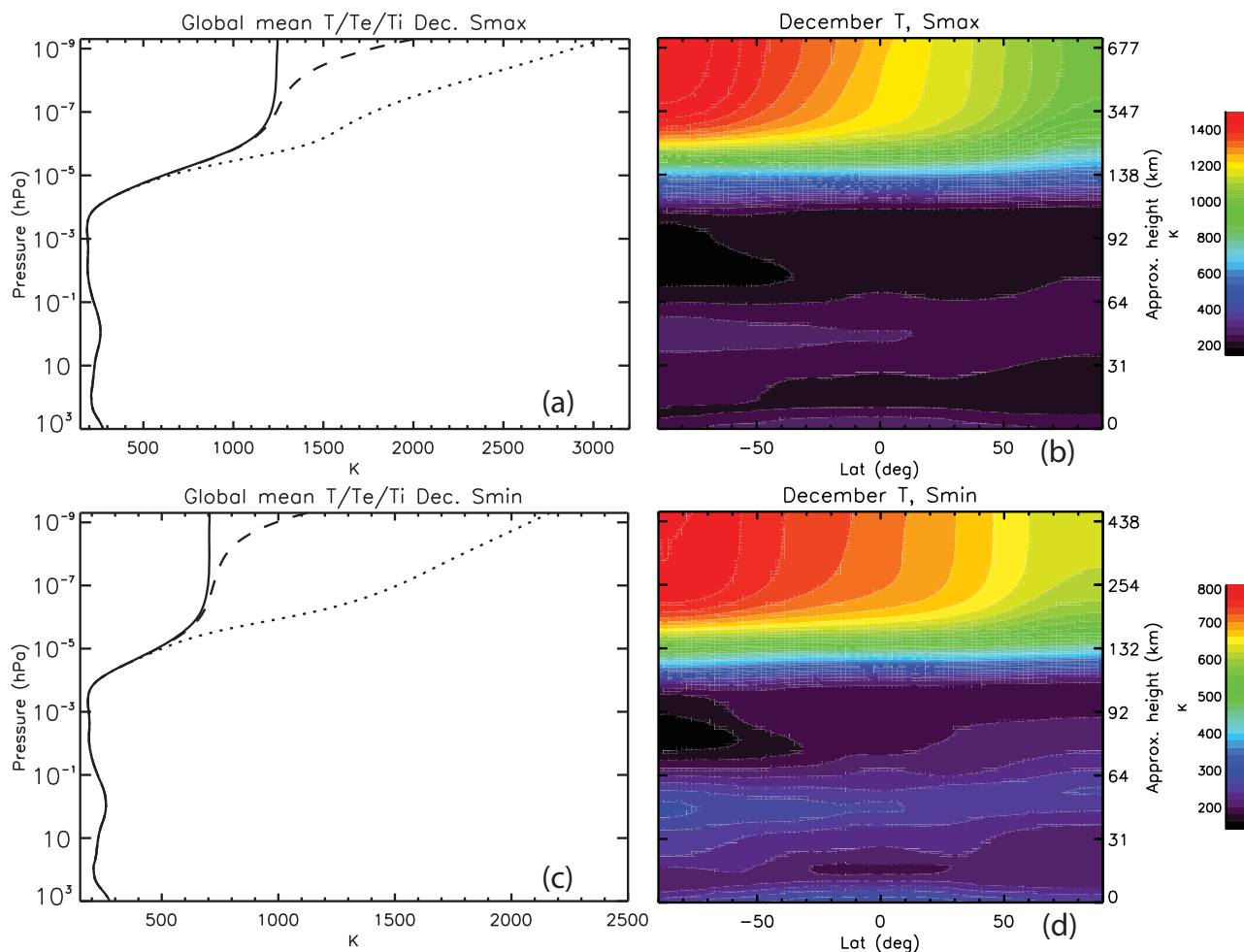
Figure 2. Monthly averaged global mean temperature (solid lines), electron temperature (dotted lines), and ion temperatures (dashed lines) for December from WACCM-X simulations under (a) solar maximum and (c) solar minimum conditions. The corresponding zonal mean neutral temperatures are shown in (b) and (d).
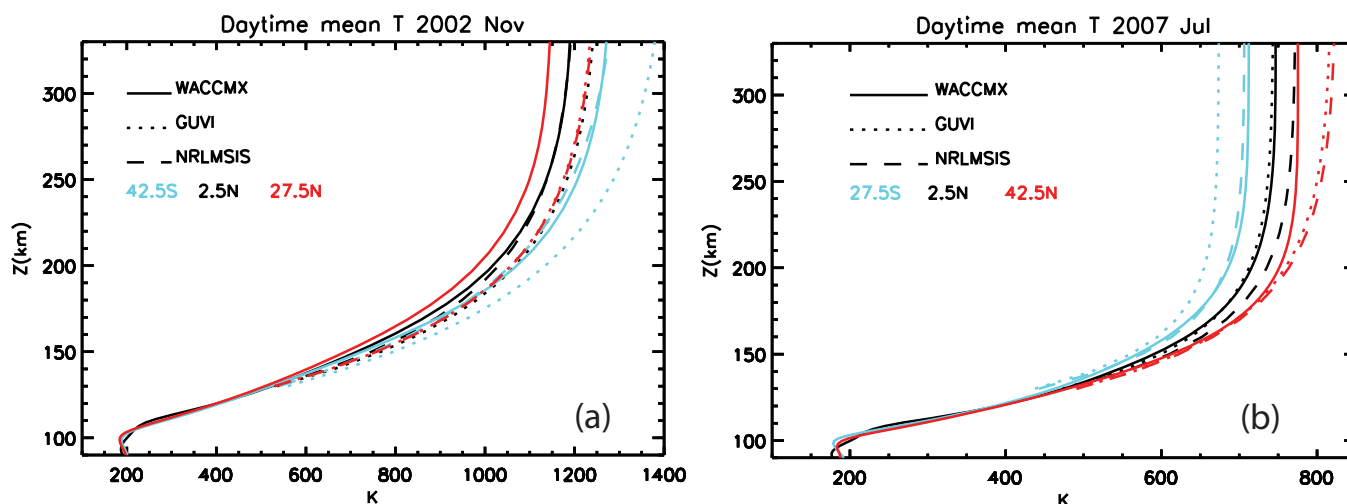
Figure 3. Neutral temperature from WACCM-X simulations (solid lines) as compared with that derived from GUVI measurements (dotted lines) and NRLMSIS empirical model results for (a) November 2002 and (b) July 2007 at midlatitudes, subtropical latitudes, and equatorial latitudes.

Under solar maximum conditions, the zonal mean temperature reaches 1,493 and 978 K over the summer and winter polar regions, respectively, warmer than the mean temperatures of 1,134 and 817 K as in the previous version of the model (without heating by thermal electrons and ions). Under solar minimum conditions, these values are 782 and 615 K, and again warmer than those from the old model version. The meridional temperature gradients from the summer to the winter hemisphere are also larger and in better agreement with the TIME-GCM results in the new version of the model.

Figures 3a and 3b compare the vertical temperature profiles from WACCM-X with GUVI measurements and the NRLMSIS empirical model under 2002 solar maximum and 2007 solar minimum conditions. GUVI temperature measurements are day time mean values averaged over one yaw cycle centered around 18 November 2002 and 15 July 2007, respectively. The model temperatures are interpolated to local times, and then averaged zonally, over day time (0800–1700 local time $<$) and over 20 days around 18 November 2002 and 15 July 2007. Three latitudes are chosen for comparison: 42.5° in the summer hemisphere, the equator (2.5°N), and 27.5° in the winter hemisphere. Under solar maximum conditions (Figure 3a), WACCM-X temperature is cooler than GUVI in the upper thermosphere, by about 100, 50, and 80 K at 42.5°S, the equator, and 27.5°N, respectively; and agrees with NRLMSIS at 42.5°S and the equator. On the other hand, GUVI and NRLMSIS temperatures agree at 27.5°N. Under solar minimum conditions (Figure 3b), WACCM-X temperature agrees with GUVI measurement at the equator (both 25 K colder than NRLMSIS), but warmer/colder than GUVI measurements by 40K/50 K at 27.5°S/42.5°N. At 27.5°S WACCM-X and NRLMSIS temperatures are similar, while at 42.5°N NRLMSIS and GUVI temperatures are similar.

The two major thermospheric neutral species calculated by WACCM-X, O and N_2, are compared with GUVI and NRLMSIS (Figure 4). Only comparisons at the equator are shown; comparisons at other latitudes are similar. Under solar maximum conditions, O number density from WACCM-X is about 15% larger than GUVI but agrees with NRLMSIS at 150 km. At higher altitudes, O from WACCM-X becomes slightly less than NRLMSIS and its difference with GUVI O decreases. N_2 number density from WACCM-X is generally larger than GUVI and NRLMSIS, but the differences between the three decrease with increasing altitude. At 150 km, WACCM-X N_2 is about 45% higher than GUVI and slightly larger than NRLMSIS, and at 330 km the three are the same. Under solar minimum conditions, O number density from WACCM-X is consistently larger than that of GUVI and NRLMSIS. At 150 km, WACCM-X O is 58% and 33% larger than GUVI and NRLMSIS O, respectively. The percentage difference between WACCM-X and GUVI is similar at higher altitudes, while the difference between WACCM-X and NRLMSIS decreases to about 20% at 330 km. WACCM-X N_2 number density, on the other hand, agrees rather well with that of GUVI and NRLMSIS. Below (above) ~270 km GUVI values are slightly less (larger) than WACCM-X and slightly larger (less) than NRLMSIS.

O number density peaks in the lower thermosphere region (~95 km). In the WACCM-X solar minimum simulation, the peak global mean O number density is 3.9×10^{11} cm^{-3} (March average), 4.4×10^{11} cm^{-3}
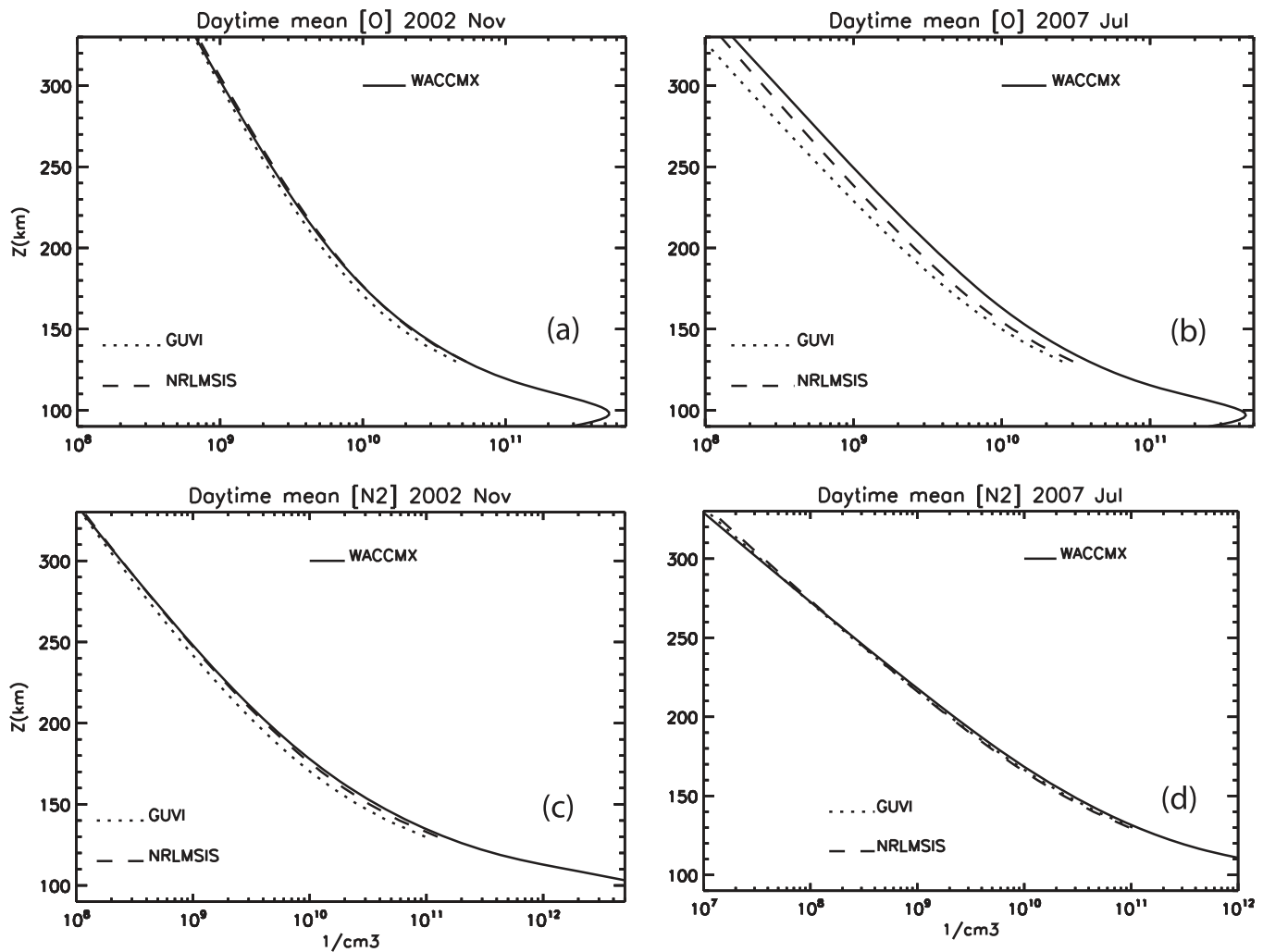
Figure 4. Similar to Figure 3, but comparing (a, b) O and (c, d) N_2 number densities for (a, c) solar maximum and (b, d) solar minimum conditions.

(June average), 4.1×10^{11} cm^{-3} (September average), and 4.4×10^{11} cm^{-3} (December average). The peak global mean O number density is larger under solar maximum conditions and displays more seasonal variability: 4.4×10^{11} cm^{-3} (March average), 5.3×10^{11} cm^{-3} (June average), 4.9×10^{11} cm^{-3} (September average), and 5.8×10^{11} cm^{-3} (December average). These values are comparable to the values obtained from previous observations by WINDII, OSIRIS, and SCIAMACHY (Kaufmann et al., 2014; Russell et al., 2005; Sheese et al., 2011), but they are less than the published SABER values (Kaufmann et al., 2014; Mlynczak et al., 2013; Smith et al., 2010). Recently, a new version of SABER night time atomic oxygen has been released. It is based on rate coefficients accounting for the recently discovered large quenching rates of highly vibrationally excited OH by atomic oxygen (Sharma et al., 2015). The new atomic oxygen profiles are approximately 25% smaller (global average) than those from the previous version (M. G. Mlynczak and J. M. Russell, personal communication, 2017). The WACCM-X results are thus close to the new SABER analysis.

Thermospheric mass density is compared with observations. Figure 5 is the neutral mass density at 400 km averaged over September (for UT0) from the solar maximum simulation (plotted over geomagnetic latitude and geographic longitude/local time). The maximum density is $\sim 1.1 \times 10^{-11}$ kg m^{-3} at around 1430 LT, and displays two peaks at $\sim 25°$ north and south of the magnetic equator. This density structure, referred to as the equatorial mass density anomaly (EMA) or equatorial thermosphere anomaly (ETA), is generally consistent with the density obtained from CHAMP measurements for September (e.g., Liu et al., 2007), though the primary peak of the latter is found around local noon. EMA is also produced by GAIA model (the ground to topside model of the atmosphere and ionosphere for aeronomy), which takes into account of ion-neutral
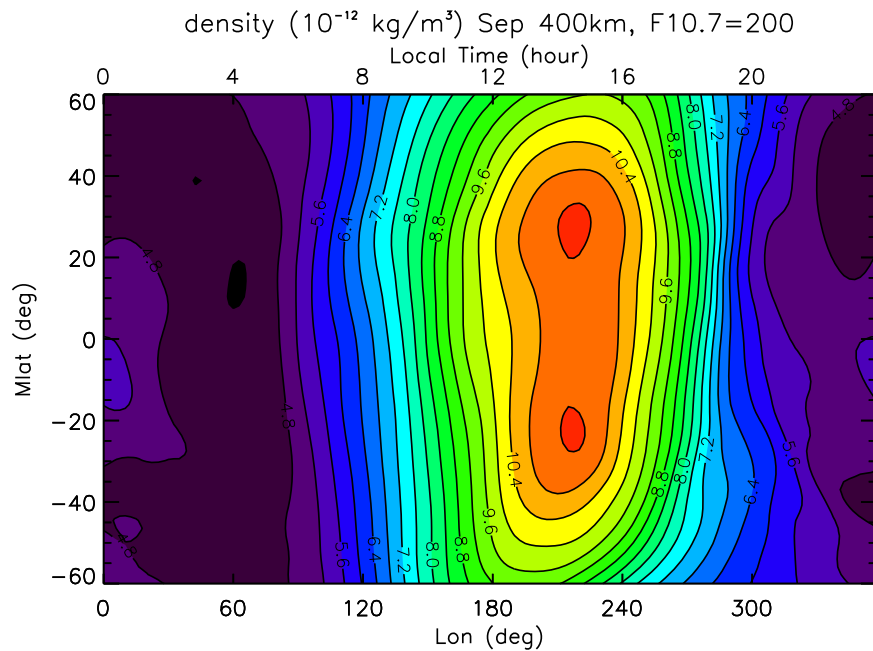
Figure 5. Neutral atmosphere density at 400 km altitude for September from WACCM-X simulations under solar maximum conditions. Contour intervals: 0.4×10^{-12} kg m^{-3}.

coupling (Miyoshi et al., 2011). In GAIA, EMA forms around 1400 LT. A study by Lei et al. (2012) concluded that heating from plasma-neutral collisions and field-aligned ion drag are the major causes of the EMA/ETA. At midnight, the density around the magnetic equator shows a local maximum of $\sim 5.6 \times 10^{-12}$ kg m^{-3}. The structure is similar to the midnight density maximum (MDM) obtained from CHAMP measurements (Ruan et al., 2014).

Figure 6 shows the variation of the global mean mass density at 400 km from the solar maximum and solar minimum simulations. Under solar maximum conditions, the global mean mass density varies between 6 and 8.5×10^{-12} kg m^{-3} with the maximum in January and minimum in May–June. Under solar minimum
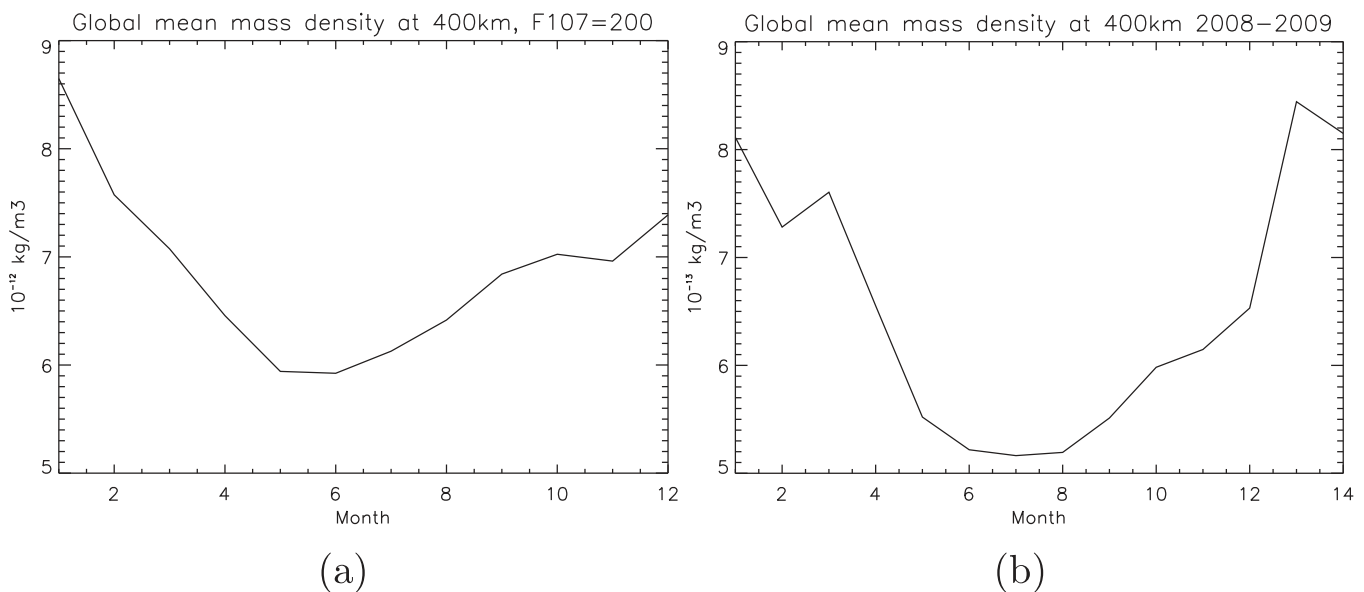
Figure 6. Monthly averaged global mean mass density at 400 km over one WACCM-X model-year under (a) solar maximum conditions and (b) solar minimum conditions (including January and February 2009). Note that the density unit is 10^{-12} kg m^{-3} in Figure 6a and 10^{-13} kg m^{-3} in Figure 6b.

conditions, the global mean mass density varies between 5 and 8 $\times 10^{-13}$ kg m^{-3} with the maximum in January and minimum in June–August. The latter is somewhat larger than the density derived from observations for 2008 (Qian & Solomon, 2012), which varies between 3 and 7 $\times 10^{-13}$ kg m^{-3}. The global mean mass density in Figure 6a is larger than the density derived from satellite drag for 2003 (2.5–4 $\times 10^{-12}$ kg m^{-3}; Qian & Solomon, 2012). Given the annual average of F10.7 flux for 2003 of $\sim$128, the annual average global mean mass density estimated from interpolating between our solar maximum run (with F10.7 set to 200) and solar minimum run (annual average of F10.7 flux = 69) would be 3.3 $\times 10^{-12}$ kg m^{-3}, which is consistent with the derived values. Although the mean values of the global mean mass density are reasonable and display an annual variation, they do not show the observed semiannual variation.

3.2. Seasonal and Short-Term Variability of Tides

With the change in divergence damping scheme (section 2.1.2), the numerical damping of tides has been reduced, and the tidal amplitudes (including migrating diurnal, semidiurnal, and terdiurnal tides) all become larger. Figures 7a and 7b are the monthly averaged zonal and meridional wind components of migrating semidiurnal tide (SW2) at $\sim$95 km. The amplitudes of both components reach maximum in the winter hemisphere (at $\sim$50° latitude). For this specific simulation year, the zonal wind amplitude is over 40 m s^{-1} at 50°N in January, and 36 m s^{-1} at 50$^-$S in May, and the maximum meridional wind amplitude is over 40 m s^{-1} for both months. A secondary peak is seen in the summer hemisphere at similar latitudes (amplitudes are 20–24 m s^{-1}). These seasonal and latitudinal features of SW2 compare well with TIDI observations (Wu et al., 2011). This seasonal dependence of SW2 in the lower thermosphere is also found in the temperature tide from SABER observations and is reproduced by the Whole Atmosphere Model (WAM; albeit with amplitudes larger than observational climatology; Akmaev et al., 2008).

Nonmigrating tides play an important role in driving thermosphere and ionosphere variability. Figure 8 shows the variation of two nonmigrating tidal components over latitude and season: the diurnal eastward-propagating zonal wave number 3 (DE3) and semidiurnal eastward-propagating zonal wave number 2 (SE2). The zonal wind amplitudes, along with their standard deviation (over each month), are shown for the altitude of $\sim$135 km. This altitude is chosen since it is near the E-region peak of the Pedersen conductivity in the early morning. The wind perturbations may thus play an important role in ionospheric wind dynamo. The DE3 amplitude is generally symmetric with respect to the equator, and peaks around August (14 m s^{-1}). This is consistent with the DE3 at this altitude derived from Hough model extension (HME) fitting of SABER and TIDI measurements (Oberheide et al., 2009). The standard deviation of the amplitude is $\sim$4 m s^{-1} over the equator throughout the year. At this altitude, the amplitude of SE2 is comparable to that of DE3, although it has different latitude and seasonal structures, with peaks between 30° and 40° latitude and around equinox. At equatorial latitudes (within 10° of the equator), the amplitude of SE2 is below 4 m s^{-1} during most time of the year
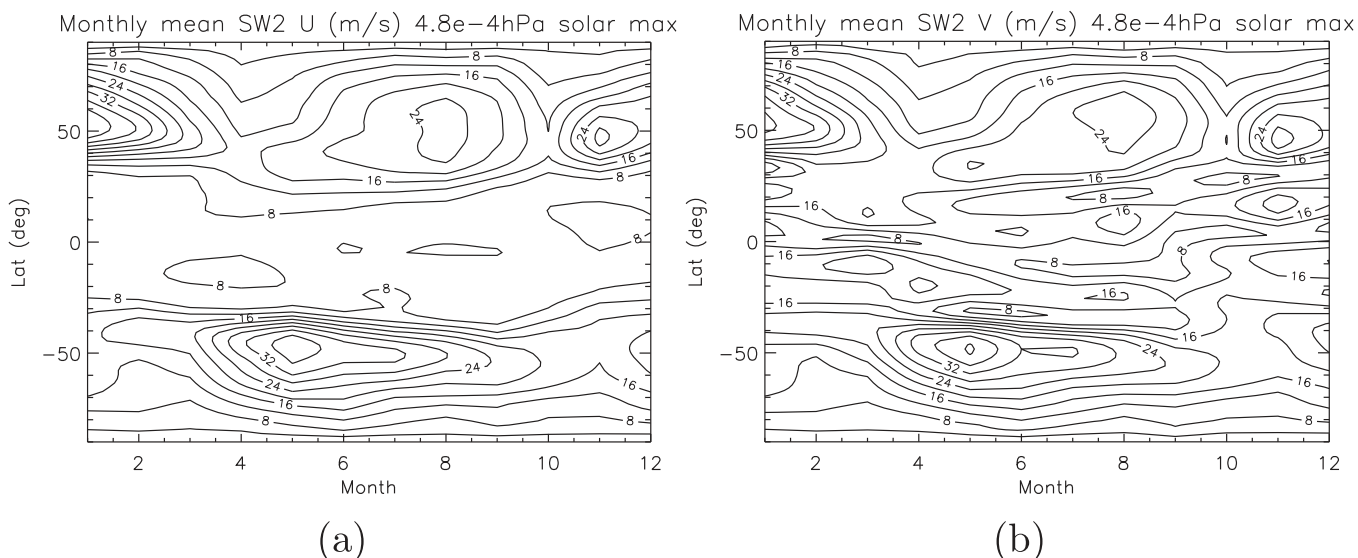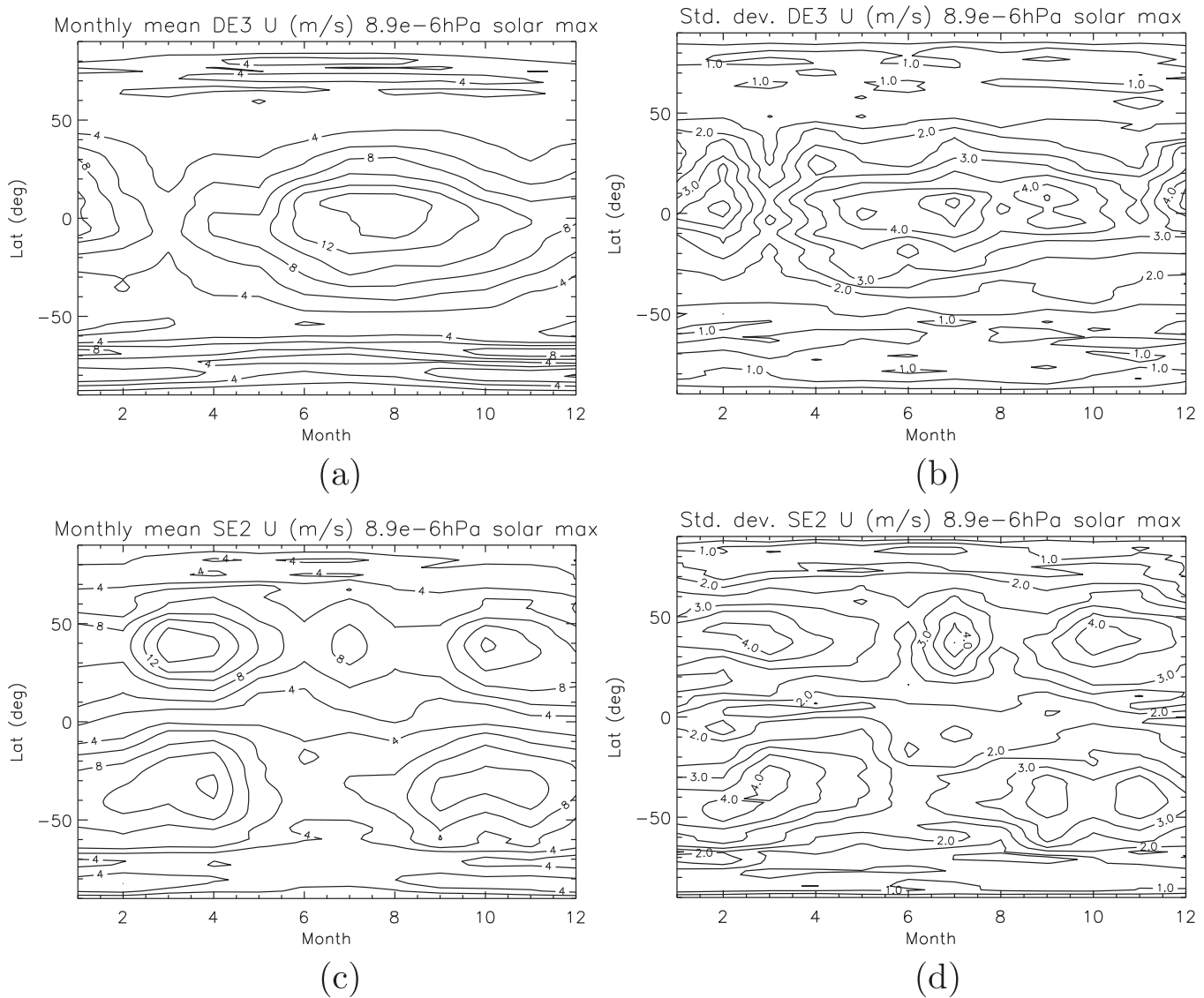

Figure 7. Monthly averaged (a) zonal and (b) meridional wind components of migrating semidiurnal tide (SW2) at $\sim$95 km. Contour intervals: 4 m s^{-1}.

Figure 8. (a, b) Monthly averaged zonal wind amplitude of nonmigrating diurnal eastward-propagating zonal wave number 3 (DE3) tide and its standard deviation, respectively, at ~135 km. (c, d) Similar to Figures 8a and 8b but for nonmigrating semidiurnal eastward-propagating zonal wave number 2 (SE2) tide. Contour intervals: 2 m s^{-1} (Figures 8a and 8c) and 1 m s^{-1} (Figures 8b and 8d).

and peaks around December. Its amplitude at the equator is about 1/5 of the DE3 amplitude in August, when the latter peaks. This is qualitatively similar to that from the nonmigrating tidal analysis of CHAMP observations for the equatorial region and at 400 km by Häusler and Lühr (2009). The standard deviation of SE2 of ~4 m s^{-1} is seen at places where the zonal wind amplitude peaks.

### 3.3. Ionospheric Structure and Variability
3.3.1. Plasma E × B Drifts

The ionospheric E × B drifts are calculated in the interactive ionospheric wind dynamo module. Figure 9 shows the vertical and zonal components of the E × B drifts under solar maximum and geomagnetic quiet conditions at 4.6 × 10^{-8} hPa (~380 km altitude) and 12.3°S/77.5°W, near the location of the Jicamarca Radio Observatory (JRO). Climatological drifts above JRO, as described by Fejer et al. (1991), are included in the figure for direct comparison. As noted in Fejer et al. (1991), these values represent averages usually between 300 and 400 km, and the average F10.7 values for equinox (March–April and September–October), winter (May–August), and summer (November–February) were 194, 174, and 168, respectively. Both daily (grey lines) and average (black lines) from model simulations are shown. The vertical component of
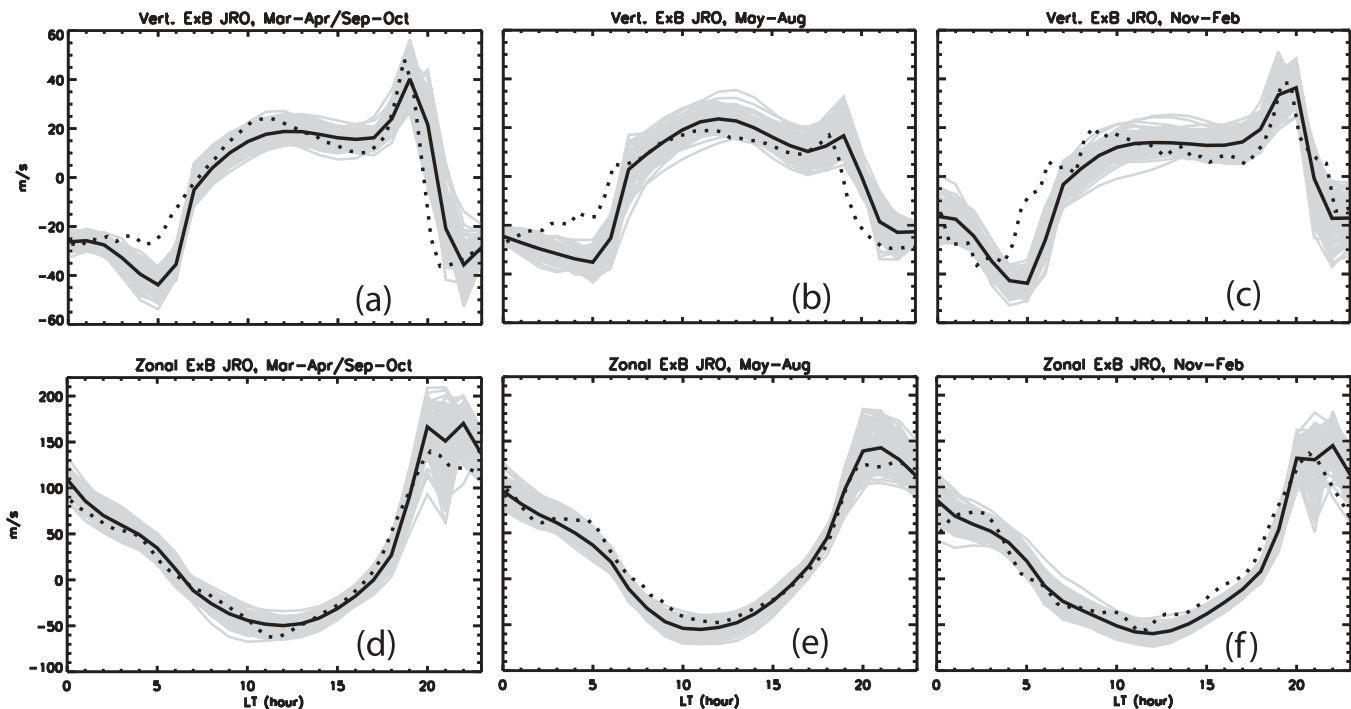
Figure 9. (a–c) Vertical and (d–f) zonal components of E × B drifts for the time periods of equinoxes (March–April and September–October), southern winter (May–August), and northern winter (November–February), respectively. Black/grey lines: average/daily model values over the respective time periods at 12.3°S/77.5°W and ∼380 km. Dotted lines: climatological drift values obtained from JRO observations (Fejer et al., 1991). F10.7: 200 sfu for model simulations; 194, 174, and 168 sfu for JRO equinoctial, winter, and summer observations, respectively.

the E × B drift from the model show general agreement with the JRO observations (Figures 9a–9c). The magnitude of the simulated daytime upward drift is similar to that of the observed, but the timing of the daytime extrema is different, with the latter occurring somewhat earlier. At dusk, the magnitude of the pre-reversal enhancement (PRE) and its seasonal variation are comparable between the simulation and the climatology, with the largest average PRE found around equinoxes (∼40 m s^{-1} in simulations and ∼48 m s^{-1} in observations). The timing of PRE is similar between the two around equinoxes (1900 LT) and summer (around 1930 LT), though the simulated PRE lags the climatology by ∼40 min during winter. The downward drifts before midnight are similar and display similar seasonal variation. However, the simulated downward drifts continue to grow from midnight till dawn and reach maximum values at LT 5–6 h, which is not seen in the climatology. As a result, the transition of vertical drift from downward to upward after dawn occurs later and is more abrupt in the simulations. The scattering of the daily values around the mean ranges from 5 to 15 m s^{-1}, similar to those obtained from observations (Scherliess & Fejer, 1999). The scattering reflects the day-to-day variability of the drifts, and in the simulations it is caused entirely by variability from the lower atmosphere, since Kp is held constant. This is consistent with previous studies, using TIME-GCM, TIE-GCM, and WAM (Fang et al., 2013; Liu et al., 2013; Maute, 2017). A variable Kp would introduce additional scattering, even for fairly quiet days. It is noted that gravity-driven ionospheric current, which is not included in the electrodynamic solver, can lead to additional vertical drift changes by several m s^{-1} (Eccles, 2004; Maute et al., 2012).

The zonal E × B drift from the model is also in agreement with climatology at JRO (Figures 9d–9f). The westward drift during daytime reaches maximum value of 50–60 m s^{-1} at local noon, and the eastward drift during nighttime reaches maximum value between 130 and 170 m s^{-1} at LT 21–22 h. This day-night asymmetry of zonal drift results from the day-night difference of the polarization field, as discussed by Rishbeth (2002). The phase of the zonal drift, including the time it turns from eastward to westward in the morning and back to eastward in the later afternoon, and their seasonal dependence are comparable between the simulations and the climatology. The scattering of the zonal drift is between 20 and 50 m s^{-1} at most local times, similar to the observations (Fejer et al., 2005). Like the vertical drifts, the zonal drifts also display
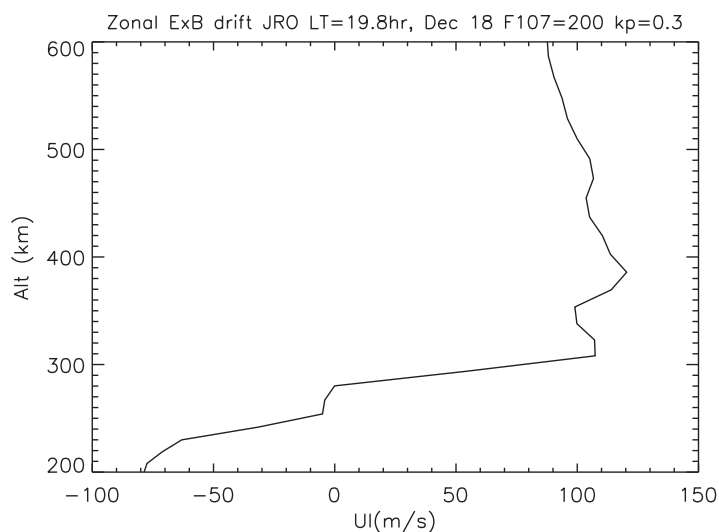
Figure 10. Vertical profile of zonal E × B drift at 12.3°S/77.5°W and 1948 LT on 18 December of the simulation under solar maximum conditions.

large day-to-day variability. As demonstrated in previous studies, this is associated with the variability of the neutral zonal wind (e.g., Miyoshi et al., 2012).

The vertical structure of the simulated zonal drift is shown in Figure 10, also at the location of JRO and 1948 LT. The zonal drift reaches a maximum of eastward 120 m s^{-1} between 300 and 400 km. Between 200 and 300 km, the zonal drift has a large eastward shear, increasing from -80 to 110 m s^{-1}. This vertical structure is similar to the observed one over JRO (Hysell et al., 2015) and is caused primarily by the vertical shear of the zonal wind (Richmond et al., 2015).

Simulated vertical E × B drift under solar minimum conditions (2008) is validated against various observations by Liu et al. (submitted manuscript, 2017), and general agreement is found. The main discrepancy is that the downward drift after midnight and before dawn is too strong in the simulation, as under solar maximum conditions. The local time dependence of the zonal E × B drift under solar minimum conditions is similar to climatology (Fejer et al., 2005). The night time eastward drift maximum in the simulation ($\sim$60 m s^{-1}) is weaker than climatology (90–100 m s^{-1}). It is noted, however, the solar F10.7 radio flux used for obtaining the drift climatology under solar minimum conditions in (Fejer et al., 2005) was 80 sfu, while the mean F10.7 flux value for 2008 was 68 sfu. The weaker maximum eastward drift is thus likely a result of lower solar activity in 2008.

As noted in previous studies (e.g., Basu et al., 1996; Fejer et al., 1999), the strength of PRE is closely associated with the development of equatorial spread-F (ESF). The seasonal, longitudinal, and solar activity dependence of ESF occurrence frequency are similar to those of the maximum PRE (Gentile et al., 2006; Huang & Hairston, 2015; Kil et al., 2009). It is thus important for global models to reproduce such dependencies of maximum PRE to provide the large-scale conditions for ESF models. Figure 11a shows the longitudinal and seasonal structures of monthly averaged maximum PRE (calculated as the maximum vertical drift between 14°S and 14°N and 1700–2000 LT at each longitude) from the solar maximum simulation. From months around December solstice (November–February), the strongest PRE (50–60 m s^{-1}) are found between 20 and 70°W (American sector and the Atlantic), while the lowest PRE (20–30 m s^{-1}) are around $\sim$130°W and 110°E. Around March solstice (February–May), strong PREs become more broadly distributed over longitude, with the peak values shifting both eastward and westward. During March–April, the strongest PREs are found around 0 longitude and 100°W. An additional, somewhat weaker peak ($\sim$40 m s^{-1}) is seen around 140°E. Around June solstice (May–August), the maximum PREs are located around 20°E and the international date line, with values of $\sim$30 m s^{-1}, weaker than the maximum values between November and February. Between these two peaks and in both eastern and western hemispheres, the local maximum PREs are lowest of the whole year, between 10 and 20 m s^{-1}. The PRE variation from August to December is opposite to the variation around March equinox. The seasonal and longitudinal variations of the maximum PRE under solar minimum conditions (Figure 11b) are similar to those under solar maximum conditions, but the upward drift values are much lower under solar minimum conditions. The seasonal and longitudinal variations and their dependence on solar activity are in good agreement with drift observations (e.g., Huang & Hairston, 2015; Kil et al., 2009), and with the seasonal and longitudinal variations of ESF occurrence (e.g., Gentile et al., 2006).

Figures 11c and 11d are the daily values of maximum PRE (so Figures 11a and 11b are their monthly averages). It is evident from these two figures that the maximum PRE varies significantly from day-to-day, and the daily PRE can be much stronger (or weaker) than the climatological values. For example, around June solstice under solar maximum conditions, the daily values of maximum PRE can sometimes reach 40 m s^{-1} or stronger at longitudes where their monthly mean values are 20 m s^{-1} or less. The day-to-day variability of the PRE is expected to be even larger with variable geomagnetic conditions (Kp). It may have important implications for understanding why ESF does or does not occur on a specific day, and its causes warrant more detailed investigation in the future.
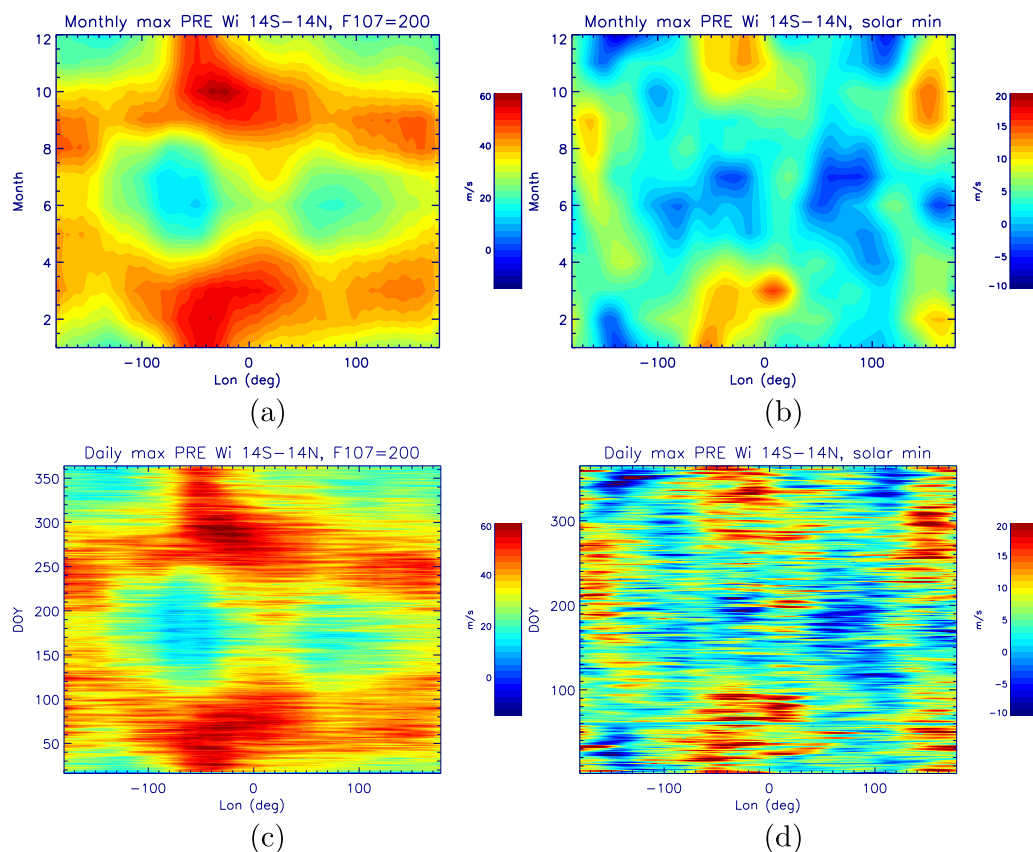
Figure 11. (a,b) Monthly averaged values of maximum prereveral enhancement (PRE) between 14°S and 14°N from WACCM-X simulations under solar maximum and solar minimum conditions, respectively. (c, d) Similar to Figures 11a and 11b but daily values of PRE.

3.3.2. Ionospheric Structure

The electron density at 400 km from the simulation under solar maximum conditions is shown in Figure 12 (monthly average over September is shown). The equatorial ionization anomaly (EIA) structure is reproduced (Appleton, 1946). The EIA is generated by the fountain effect due to the upward vertical drift associated with eastward electric fields produced by the ionospheric E-region dynamo. The EIA crests are at $\sim15°$ geomagnetic latitude with a valley around the dip equator. They extend from the morning sector to midnight, with maximum values ($\sim3.2\times10^6$ cm^{-3}) around 1600 LT. Two deep equatorial electron density minima are seen around dawn and dusk ($1-2\times10^5$ cm^{-3}). These features are similar to the electron density at 400 km measured by CHAMP (Liu et al., 2005). Detailed comparisons of F-region peak height and density (hmF2 and NmF2) between model results and COSMIC observations have been made by Liu et al. (submitted manuscript, 2017). While the general morphologies of hmF2 and NmF2 from the model are similar to those deduced from observations, the simulated NmF2 is systematically lower. One possible cause of this underestimation is that the eddy diffusion by the current gravity wave parameterization scheme becomes too large and continues to grow with altitude till ~200 km. Sensitivity tests demonstrate that reduction of the eddy diffusion above the turbopause leads to an increase of ionospheric density in F-region.

3.3.3. Storm Time Ionospheric Responses

WACCM-X is now capable of simulating atmospheric responses to geomagnetic storms. Figure 13 illustrates global maps of ionospheric F2-region peak density (NmF2) from WACCM-X during both geomagnetic quiet (magnitudes of IMF B$_y$ and B$_z$ are less than 5 nT, bottom, 16 March 2013) and storm conditions (magnitude of IMF B$_z$ is about -10 nT, and SYM-H is close to -130 nT, top, 17 March 2013). Under geomagnetic quiet condition, a well-defined EIA is seen in NmF2, similar to the electron density structure at 400 km (Figure 12).

During the geomagnetic storm period, the EIA crests expanded to higher latitudes ($\sim25°$) in the morning to noon sector. The poleward expansion of EIA crests could be related to the prompt penetration electric fields
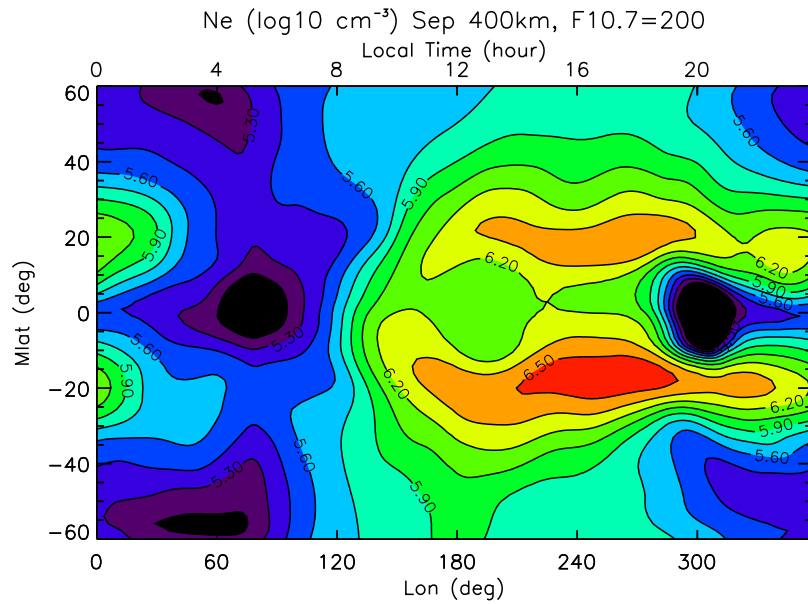
Figure 12. Electron density at 400 km altitude for September from WACCM-X simulations under solar maximum conditions.

enhancing daytime fountain effects (e.g., Lu et al., 2012; Wang et al., 2010). Another noteworthy feature is the poleward extension of positive storm effects termed as storm-enhanced density (SED) which was identified as a relatively narrow enhanced TEC structure within the 40°–60° latitudinal range and between 1100 and 1200 LT (over the east coast of Canada). SED is a special category of the positive storm effect in the
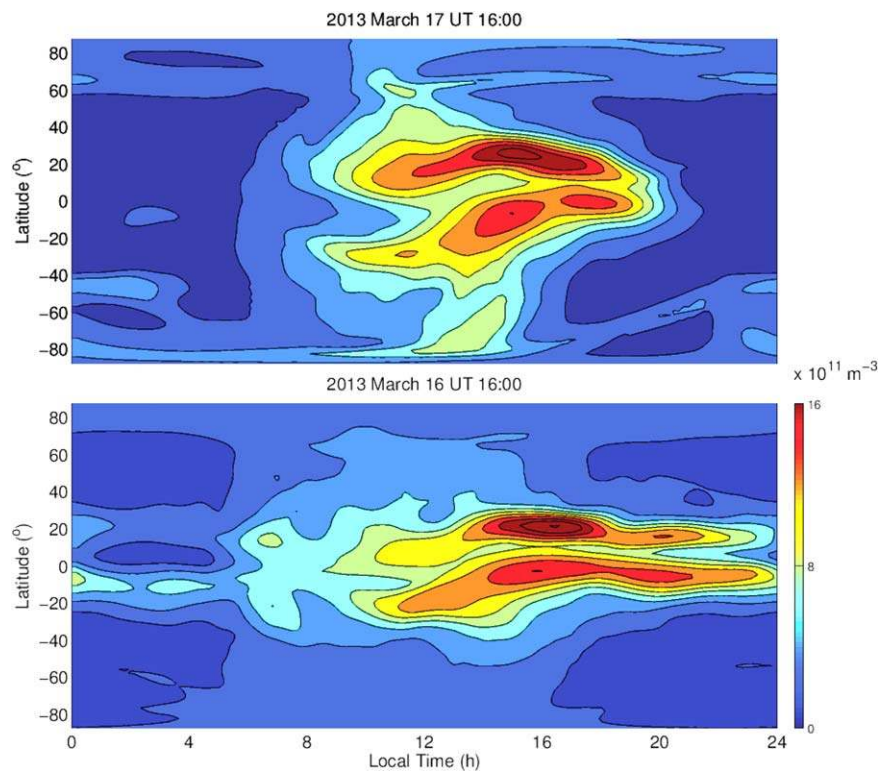
Figure 13. Global view of WACCM-X simulated NmF2 at 1900 UT during storm time (17 March 2013) and quiet time (16 March 2013).

premidnight and afternoon sectors at the equatorward and westward edge of the middle latitude iono-spheric electron density trough and is more likely to appear over North America. SED is mainly caused by the local upward ion drifts reducing chemical recombination and increasing electron density (Liu et al., 2016a, 2016b). Tongue of ionization (TOI) seen poleward of 60° latitude can be viewed as the extension of SED due to horizontal transport by high-latitude convection. TOI structures show nearly hemispheric sym-metry and can be seen in both the Northern Hemisphere and Southern Hemisphere. These salient spatial structures from WACCM-X, including the poleward expansion of EIA, SED and TOI, are similar to GPS TEC observations (e.g., Liu et al., 2016b).

4. Summary and Future Plans

The development of WACCM-X to implement a coupled ionosphere, including self-consistent low-mid-lati-tude electrodynamics is described above. As illustrated by the results in section 3, the current version of WACCM-X is capable of reproducing the climatological ionosphere-thermosphere state, as well as variability on hourly to daily time scales due to both geomagnetic and lower atmosphere forcing. Despite the general agreement of our current model with the climalogical ionosphere and thermosphere features, we envisage several areas of further improvements. More specifically, areas of active model development which we believe will considerably enhance the scientific value of WACCM-X simulation results are briefly detailed in the following.

WACCM-X is currently limited in its ability to simulate geomagnetic activity due to the use of the Heelis con-vection pattern at high-latitudes. There exist alternative methods for specifying the high-latitude electric potential and auroral precipitation. These include the Weimer (2005) empirical model driven by observed upstream IMF conditions, as well as data assimilative schemes such as the Assimilative Mapping of Iono-sphere Electrodynamics (AMIE) procedure (Richmond & Kamide, 1988). Implementation of these alternative methods for high-latitude forcing specification will lead to improved simulations of storm time ionosphere-thermosphere variability.

Pedatella et al. (2014) implemented the data assimilation capability into WACCM using the Data Assimila-tion Research Testbed (DART) ensemble Kalman filter. This work is currently being extended to WACCM-X so that the model meteorology can be constrained by the assimilation of lower and middle atmosphere observations. This will enhance the capability of the model to reproduce ionosphere-thermosphere variabil-ity driven by the lower atmosphere. In the future, data assimilation will be extended into the upper atmo-sphere through assimilation of ground and satellite observations, such as from the upcoming COSMIC-2, GOLD, and ICON satellite missions. This will further constrain the model state, leading to a whole atmosphere-ionosphere reanalysis.

WACCM-X is built upon the chemistry, dynamics, and physics of CAM4 and WACCM4. Both CAM and WACCM have seen their own significant recent developments, including increased horizontal resolution, and CAM6 and WACCM6 will be released as part of CESM 2.0. The latest versions of CAM and WACCM addi-tionally include updated convection and gravity wave drag parameterization schemes. These can indirectly impact the upper atmosphere through improved representation of middle atmosphere circulation, as well as better simulation of tidal forcing and variability due to latent heating. Future versions of WACCM-X will incorporate the recent improvements in the lower and middle atmosphere components of CESM.

The current WACCM-X grid resolution inhibits the investigation of mesoscale structures, as well as coupling between small-scale and large-scale variability. These can have significant impact on the upper atmosphere (e.g., Liu, 2016, and references therein). Liu et al. (2014) developed a high resolution (∼0.25° horizontally, and 0.1 scale height vertically) version of WACCM. Development of a high resolution version of WACCM-X will enable an enhanced understanding of the potential impact of mesoscale structures on the ionosphere-thermosphere system.

WACCM-X 2.0 is being released as an optional configuration of CESM 2.0. It currently is installed on the NCAR supercomputers and is available to any researcher with access to those machines. It is an open-source community model, which can be installed on any computer of sufficient capability that supports the necessary compilers and libraries. Porting the model to other environments can be accomplished by access-ing the information at the NCAR CESM web site and related support pages and will be supported once

CESM 2.0 is officially released. Due to the complexity of WACCM-X, its many interlinked components, and the larger world of Earth system modeling on which it is based, participation in development is solicited from researchers in various fields. Much work lies ahead to compare, validate, and improve the model through comparisons with observations, empirical models, and other numerical models. To this end, SD WACCM-X simulation results for 2000–2009 have been made available for community use via https://www.earthsystemgrid.org (Earth System Grid).

References

Akmaev, R. A. (2011). Whole atmosphere modeling: Connecting terrestrial and space weather. *Reviews of Geophysics*, *49*, RG4004. https://doi.org/10.1029/2011RG000364

Akmaev, R. A., Fuller-Rowell, T. J., Wu, F., Forbes, J. M., Zhang, X., Anghel, A. F., et al. (2008). Tidal variability in the lower thermosphere: Comparison of Whole Atmosphere Model (WAM) simulations with observations from TIMED. *Geophysical Research Letters*, *35*, L03810. https://doi.org/10.1029/2007GL032584

Appleton, E. V. (1946). Two anomalies in the ionosphere. *Nature*, *157*, 691–693.

Basu, S., Kudeki, E., Basu, S., Valladares, C. E., Weber, E. J., Zengingonul, H. P., et al. (1996). Scintillations, plasma drifts, and neutral winds in the equatorial ionosphere after sunset. *Journal of Geophysical Research: Space Physics*, *101*, 26795–26809. https://doi.org/10.1029/96JA00760

Bates, D. R. (1951). The temperature of the upper atmosphere. *Proceedings of the Physical Society of London, Section B*, *64*, 805.

Bilitza, D. (2001). International Reference Ionosphere 2000. *Radio Science*, *36*, 261–275. https://doi.org/10.1029/2000RS002432

Chamberlin, P. C., Woods, T. N., & Eparvier, F. G. (2007). Flare Irradiance Spectral Model (FISM): Daily component algorithms and results. *Space Weather*, *5*, S07005. https://doi.org/10.1029/2007SW000316

Chamberlin, P. C., Woods, T. N., & Eparvier, F. G. (2008). Flare Irradiance Spectral Model (FISM): Flare component algorithms and results. *Space Weather*, *6*, S05001. https://doi.org/10.1029/2007SW000372

Eccles, J. V. (2004). The effect of gravity and pressure in the electrodynamics of the low-latitude ionosphere. *Journal of Geophysical Research: Space Physics*, *109*, A05304. https://doi.org/10.1029/2003JA010023

Emery, B. A., Roble, R. G., Ridley, E. C., Richmond, A. D., Knipp, D. J., Crowley, G., et al. (2012). *Parameterization of the ion convection and the auroral oval in the ncar thermospheric general circulation models* (Tech. Rep. NCAR/TN-491+STR). Boulder, CO: NCAR.

Eyring, V., Ean François Lamarque, P., Hess, F., Arfeuille, K., Bowman, M. P., Chipperfiel, B., et al. (2013). Overview of IGAC/SPARC Chemistry-Climate Model Initiative (CCMI) community simulations in support of upcoming ozone and climate assessments. *SPARC Newsletter*, *40*, 48–66.

Fang, T.-W., Akmaev, R., Fuller-Rowell, T., Wu, F., Maruyama, N., & Millward, G. (2013). Longitudinal and day-to-day variability in the ionosphere from lower atmosphere tidal forcing. *Geophysical Research Letters*, *40*, 2523–2528. https://doi.org/10.1002/grl.50550

Fejer, B. G., de Paula, E. R., González, S. A., & Woodman, R. F. (1991). Average vertical and zonal F region plasma drifts over jicamarca. *Journal of Geophysical Research: Space Physics*, *96*, 13901–13906. https://doi.org/10.1029/91JA01171

Fejer, B. G., Scherliess, L., & de Paula, E. R. (1999). Effects of the vertical plasma drift velocity on the generation and evolution of equatorial spread F. *Journal of Geophysical Research: Space Physics*, *104*, 19859–19869.

Fejer, B. G., Souza, J. R., Santos, A. S., & Costa Pereira, A. E. (2005). Climatology of F region zonal plasma drifts over Jicamarca. *Journal of Geophysical Research: Space Physics*, *110*, A12310. https://doi.org/10.1029/2005JA011324

Garcia, R. R., López-Puertas, M., Funke, B., Marsh, D. R., Kinnison, D. E., Smith, A. K., et al. (2014). On the distribution of CO_2 and CO in the mesosphere and lower thermosphere. *Journal of Geophysical Research: Atmospheres*, *119*, 5700–5718. https://doi.org/10.1002/2013JD021208

Garcia, R. R., Smith, A. K., Kinnison, D. E., de la Cámara, Á., & Murphy, D. J. (2017). Modification of the gravity wave parameterization in the Whole Atmosphere Community Climate Model: Motivation and results. *Journal of the Atmospheric Sciences*, *74*, 275–291. https://doi.org/10.1175/JAS-D-16-0104.1

Gentile, L. C., Burke, W. J., & Rich, F. J. (2006). A climatology of equatorial plasma bubbles from DMSP 1989–2004. *Radio Science*, *41*, RS5S21. https://doi.org/10.1029/2005RS003340

Goncharenko, L., Chau, J., Liu, H.-L., & Coster, A. J. (2010a). Unexpected connections between the stratosphere and ionosphere. *Geophysical Research Letters*, *37*, L10101. https://doi.org/10.1029/2010GL043125

Goncharenko, L., Coster, A. J., Chau, J., & Valladares, C. (2010b). Impact of sudden stratospheric warmings on equatorial ionization anomaly. *Journal of Geophysical Research: Space Physics*, *115*, A00G07. https://doi.org/10.1029/2010JA015400

Hagan, M. E., Maute, A., Roble, R. G., Richmond, A. D., Immel, T. J., & England, S. L. (2007). Connections between deep tropical clouds and the Earth's ionosphere. *Geophysical Research Letters*, *34*, L20109. https://doi.org/10.1029/2007GL030142

Häusler, K., & Lühr, H. (2009). Nonmigrating tidal signals in the upper thermospheric zonal wind at equatorial latitudes as observed by CHAMP. *Annals of Geophysics*, *27*, 2643–2652.

Heelis, R. A., Lowell, J. K., & Spiro, R. W. (1982). A model of the high-latitude ionospheric convection pattern. *Journal of Geophysical Research: Space Physics*, *87*, 6339–6345.

Huang, C.-S., & Hairston, M. R. (2015). The postsunset vertical plasma drift and its effects on the generation of equatorial plasma bubbles observed by the c/nofs satellite. *Journal of Geophysical Research: Space Physics*, *120*, 2263–2275. https://doi.org/10.1002/2014JA020735

Hurrell, J. W., Holland, M. M., Gent, P. R., Ghan, S., Kay, J. E., Kushner, P. J., et al. (2013). The Community Earth System Model: A framework for collaborative research. *Bulletin of the American Meteorological Society*, *94*, 1339–1360. https://doi.org/10.1175/BAMS-D-12-00121.1

Hysell, D. L., Milla, M. A., Condori, L., & Vierinen, J. (2015). Data-driven numerical simulations of equatorial spread F in the Peruvian sector 3: Solstice. *Journal of Geophysical Research: Space Physics*, *120*, 10809–10822. https://doi.org/10.1002/2015JA021877

Immel, T. J., Sagawa, E., England, S. L., Henderson, S. B., Hagan, M. E., Mende, S. B., et al. (2006). Control of equatorial ionospheric morphology by atmospheric tides. *Geophysical Research Letters*, *33*, L15108. https://doi.org/10.1029/2006GL026161

Kaufmann, M., Zhu, Y., Ern, M., & Riese, M. (2014). Global distribution of atomic oxygen in the mesopause region as derived from sciamachy O(1S) green line measurements. *Geophysical Research Letters*, *41*, 6274–6280. https://doi.org/10.1002/2014GL060574

Kil, H., Paxton, L. J., & Oh, S.-J. (2009). Global bubble distribution seen from ROCSAT-1 and its association with the evening prereversal enhancement. *Journal of Geophysical Research: Space Physics*, *114*, A06307. https://doi.org/10.1029/2008JA013672

Kockarts, G., & Peetermans, W. (1970). Atomic oxygen infrared emission in the Earth's upper atmosphere. *Planetary and Space Science*, *18*, 271.

Lauritzen, P. H., Mirin, A. A., Truesdale, J., Raeder, K., Anderson, J. L., Bacmeister, J., et al. (2012). Implementation of new diffusion/filtering operators in the CAM-FV dynamical core. *The International Journal of High Performance Computing Applications*, *27*(1), 63–73. https://doi.org/10.1177/1094342011410088

Lean, J., Rottman, G., Harder, J., & Kopp, G. (2005). Sorce contributions to new understanding of global change and solar variability. *Solar Physics*, *230*, 27–53. https://doi.org/10.1007/s11207-005-1527-2

Lei, J., Thayer, J. P., Wang, W., Richmond, A. D., Roble, R., Luan, X., et al. (2012). Simulations of the equatorial thermosphere anomaly: Field-aligned ion drag effect. *Journal of Geophysical Research: Space Physics*, *117*, A01304. https://doi.org/10.1029/2011JA017114

Lin, S.-J. (1997). A finite-volume integration method for computing pressure gradient force in general vertical coordinates. *Quarterly Journal of the Royal Meteorological Society*, *123*, 1749–1762. https://doi.org/10.1002/qj.49712354214

Lin, S.-J., & Rood, R. B. (1996). Multidimensional flux-form semi-Lagrangian transport schemes. *Monthly Weather Review*, *124*, 2046–2070. https://doi.org/10.1175/1520-0493(1996)124<2046:MFFSLT>2.0.CO;2

Lin, S.-J., & Rood, R. B. (1997). An explicit flux-form semi-Lagrangian shallow-water model on the sphere. *Quarterly Journal of the Royal Meteorological Society*, *123*, 2477–2498. https://doi.org/10.1002/qj.49712354416

Liu, J., Liu, H.-L., Wenbin Wang, A. G. B., Wu, Q., Gan, Q., Solomon, S. C., et al. (2017). First results from ionospheric extension of WACCM-X during the deep solar minimum year 2008. *Journal of Geophysical Research: Space Physics*, *123*. https://doi.org/10.1002/2017JA025010

Liu, H., Lühr, H., Henize, V., & Köhler, W. (2005). Global distribution of the thermospheric total mass density derived from CHAMP. *Journal of Geophysical Research: Space Physics*, *110*, A04301. https://doi.org/10.1029/2004JA010741

Liu, H., Lühr, H., & Watanabe, S. (2007). Climatology of the equatorial thermospheric mass density anomaly. *Journal of Geophysical Research: Space Physics*, *112*, A05305. https://doi.org/10.1029/2006JA012199

Liu, H.-L. (2016). Variability and predictability of the space environment as related to lower atmosphere forcing. *Space Weather*, *14*, 634–658. https://doi.org/10.1002/2016SW001450

Liu, H.-L., Foster, B. T., Hagan, M. E., McInerney, J. M., Maute, A., Qian, L., et al. (2010). Thermosphere extension of the Whole Atmosphere Community Climate Model. *Journal of Geophysical Research: Space Physics*, *115*, A12302. https://doi.org/10.1029/2010JA015586

Liu, H.-L., McInerney, J. M., Santos, S., Lauritzen, P. H., Taylor, M. A., & Pedatella, N. M. (2014). Gravity waves simulated by high-resolution Whole Atmosphere Community Climate Model. *Geophysical Research Letters*, *41*, 9106–9112. https://doi.org/10.1002/2014GL062468

Liu, H.-L., & Roble, R. G. (2002). A study of a self-generated stratospheric sudden warming and its mesospheric–lower thermospheric impacts using the coupled TIME-GCM/CCM3. *Journal of Geophysical Research: Atmospheres*, *107*(D23), 4695. https://doi.org/10.1029/2001JD001533

Liu, H.-L., Yudin, V. A., & Roble, R. G. (2013). Day-to-day ionospheric variability due to lower atmosphere perturbations. *Geophysical Research Letters*, *40*, 665–670. https://doi.org/10.1002/grl.50125

Liu, J., Wang, W., Burns, A., Solomon, S. C., Zhang, S., Zhang, Y., et al. (2016b). Relative importance of horizontal and vertical transports to the formation of ionospheric storm-enhanced density and polar tongue of ionization. *Journal of Geophysical Research: Space Physics*, *121*, 8121–8133. https://doi.org/10.1002/2016JA022882

Liu, J., Wang, W., Burns, A., Yue, X., Zhang, S., Zhang, Y., et al. (2016a). Profiles of ionospheric storm-enhanced density during the 17 March 2015 Great Storm. *Journal of Geophysical Research: Space Physics*, *121*, 727–744. https://doi.org/10.1002/2015JA021832

Lu, G., Goncharenko, L., Nicolls, M. J., Maute, A., Coster, A., & Paxton, L. J. (2012). Ionospheric and thermospheric variations associated with prompt penetration electric fields. *Journal of Geophysical Research: Space Physics*, *117*, A08312. https://doi.org/10.1029/2012JA017769

Marsh, D. R., Garcia, R., Kinnison, D., Boville, B., Sassi, F., & Solomon, S. (2007). Modeling the whole atmosphere response to solar cycle changes in radiative and geomagnetic forcing. *Journal of Geophysical Research: Atmospheres*, *112*, D23306. https://doi.org/10.1029/2006JD008306

Marsh, D. R., Mills, M. J., Kinnison, D. E., Lamarque, J.-F., Calvo, N., & Polvani, L. M. (2013). Climate change from 1850 to 2005 simulated in CESM1(WACCM). *Journal of Climate*, *26*, 7372–7391. https://doi.org/10.1175/JCLI-D-12-00558.1

Maute, A. (2017). Thermosphere-Ionosphere-Electrodynamics General Circulation Model for the ionospheric connection explorer: Tiegcm-icon. *Space Science Reviews*, *212*, 523–551. https://doi.org/10.1007/s11214-017-0330-3

Maute, A., Richmond, A. D., & Roble, R. G. (2012). Sources of low-latitude ionospheric e × b drifts and their variability. *Journal of Geophysical Research: Space Physics*, *117*, A06312. https://doi.org/10.1029/2011JA017502

Miyoshi, Y., Fujiwara, H., Jin, H., Shinagawa, H., & Liu, H. (2012). Numerical simulation of the equatorial wind jet in the thermosphere. *Journal of Geophysical Research: Space Physics*, *117*, A03309. https://doi.org/10.1029/2011JA017373

Miyoshi, Y., Fujiwara, H., Jin, H., Shinagawa, H., Liu, H., & Terada, K. (2011). Model study on the formation of the equatorial mass density anomaly in the thermosphere. *Journal of Geophysical Research: Space Physics*, *116*, A05322. https://doi.org/10.1029/2010JA016315

Mlynczak, M. G., Hunt, L. A., Mast, J. C., Thomas Marshall, B., Russell, J. M., Smith, A. K., et al. (2013). Atomic oxygen in the mesosphere and lower thermosphere derived from saber: Algorithm theoretical basis and measurement uncertainty. *Journal of Geophysical Research: Atmospheres*, *118*, 5724–5735. https://doi.org/10.1002/jgrd.50401

Neale, R. B., Richter, J. H., Park, S., Lauritzen, P. H., Vavrus, S. J., Rasch, P. J., et al. (2013). The mean climate of the Community Atmosphere Model (CAM4) in forced SST and fully coupled experiments. *Journal of Climate*, *26*, 5150–5168. https://doi.org/10.1175/JCLI-D-12-00236.1

Oberheide, J., Forbes, J. M., Häusler, K., Wu, Q., & Bruinsma, S. L. (2009). Tropospheric tides from 80 to 400 km: Propagation, interannual variability, and solar cycle effects. *Journal of Geophysical Research: Atmospheres*, *114*, D00I05. https://doi.org/10.1029/2009JD012388

Pedatella, N. M., Liu, H.-L., Richmond, A. D., Maute, A., & Fang, T.-W. (2012). Simulations of solar and lunar tidal variability in the mesosphere and lower thermosphere during sudden stratosphere warmings and their influence on the low-latitude ionosphere. *Journal of Geophysical Research: Space Physics*, *117*, A08326. https://doi.org/10.1029/2012JA017858

Pedatella, N. M., Raeder, K., Anderson, J. L., & Liu, H.-L. (2014). Ensemble data assimilation in the Whole Atmosphere Community Climate Model. *Journal of Geophysical Research: Atmospheres*, *119*, 9793–9809. https://doi.org/10.1002/2014JD021776

Picone, J. M., Hedin, A. E., Drob, D. P., & Aikin, A. C. (2002). NRLMSISE-00 empirical model of the atmosphere: Statistical comparisons and scientific issues. *Journal of Geophysical Research: Space Physics*, *107*(A12), 1468. https://doi.org/10.1029/2002JA009430

Qian, L., & Solomon, S. C. (2012). Thermospheric density: An overview of temporal and spatial variations. *Space Science Reviews*, *168*, 147–173. https://doi.org/10.1007/s11214-011-9810-z

Qian, L. Y., Burns, A. G., Chamberlin, P. C., & Solomon, S. C. (2010). Flare location on the solar disk: The effect on thermosphere and ionosphere response. *Journal of Geophysical Research: Space Physics*, *115*, A09311. https://doi.org/10.1029/2009JA015225

Qian, L. Y., Burns, A. G., Emery, B. A., Foster, B., Lu, G., Maute, A., et al. (2014). The NCAR TIE-GCM: A community model of the coupled thermosphere/ionosphere system. In J. Huba, R. Schunk, & G. Khazanov (Eds.), *Modeling the ionosphere and thermosphere system, Geophysical monograph series* (chap. 7, p. 73). Chichester, UK: John Wiley. https://doi.org/10.1002/9781118704417.ch7

Qian, L. Y., Solomon, S. C., & Kane, T. J. (2009). Seasonal variation of thermospheric density and composition. *Journal of Geophysical Research: Space Physics*, *114*, A01312. https://doi.org/10.1029/2008JA013643

Rees, M. H., & Roble, R. G. (1975). Observations and theory of the formation of stable auroral red arcs. *Reviews of Geophysics and Space Physics*, *13*, 201–242.

Rienecker, M. M., Suarez, M. J., Gelaro, R., Todling, R., Bacmeister, J., Liu, E., et al. (2011). MERRA: NASA's Modern-Era Retrospective Analysis for Research and Applications. *Journal of Climate*, *24*, 3624–3648. https://doi.org/10.1175/JCLI-D-11-00015.1

Richmond, A. D. (1995). Ionospheric electrodynamics using magnetic apex coordinates. *Journal of Geomagnetism and Geoelectricity*, *47*, 191–212.

Richmond, A. D., Fang, T.-W., & Maute, A. (2015). Electrodynamics of the equatorial evening ionosphere: 1. Importance of winds in different regions. *Journal of Geophysical Research: Space Physics*, *120*, 2118–2132. https://doi.org/10.1002/2014JA020934

Richmond, A. D., & Kamide, Y. (1988). Mapping electrodynamic features of the high-latitude ionosphere from localized observations: Technique. *Journal of Geophysical Research: Space Physics*, *93*, 5741–5759. https://doi.org/10.1029/JA093iA06p05741

Richmond, A. D., & Maute, A. (2014). Ionospheric electrodynamics modeling. In J. Huba, R. Schunk, & G. Khazanov (Eds.), *Modeling the ionosphere and thermosphere system, Geophysical monograph series* (chap. 6, pp. 57–71). Chichester, UK: John Wiley. https://doi.org/10.1002/9781118704417.ch6

Richmond, A. D., Ridley, E. C., & Roble, R. G. (1992). A thermosphere/ionosphere general circulation model with coupled electrodynamics. *Geophysical Research Letters*, *19*, 601–604.

Richter, J. H., Sassi, F., & Garcia, R. R. (2010). Toward a physically based gravity wave source parameterization in a general circulation model. *Journal of the Atmospheric Sciences*, *67*, 136–156. https://doi.org/10.1175/2009JAS3112.1

Rishbeth, H. (2002). Whatever happened to superrotation? *Journal of Atmospheric and Solar-Terrestrial Physics*, *64*, 1351–1360.

Roble, R., & Hastings, J. (1977). Thermal response properties of the Earth's ionospheric plasma. *Planetary and Space Science*, *25*, 217–231. https://doi.org/10.1016/0032-0633(77)90133-7

Roble, R. G. (1995). Energetics of the mesosphere and thermosphere. In R. M. Johnson & T. L. Killeen 9Eds.), *The upper mesosphere and lower thermosphere: A Review Of Experiment And Theory* (No. 87), *Geophysical monograph series* (p. 356). Washington, DC: American Geophysical Union.

Roble, R. G., & Ridley, E. C. (1987). An auroral model for the ncar thermosphere general circulation model (TGCM). *Annales Geophysicae*, *5A*, 369–382.

Roble, R. G., & Ridley, E. C. (1994). A Thermosphere-Ionosphere-Mesosphere-Electrodynamics General Circulation Model (TIME-GCM): Equinox solar cycle minimum simulations (30–500 km). *Geophysical Research Letters*, *21*, 417–420.

Roble, R. G., Ridley, E. C., Richmond, A. D., & Dickinson, R. E. (1988). A coupled thermosphere/ionosphere general circulation model. *Geophysical Research Letters*, *15*, 1325–1328.

Ruan, H., Lei, J., Dou, X., Wan, W., & Liu, Y. (2014). Midnight density maximum in the thermosphere from the champ observations. *Journal of Geophysical Research: Space Physics*, *119*, 3741–3746. https://doi.org/10.1002/2013JA019566

Russell, J. P., Ward, W. E., Lowe, R. P., Roble, R. G., Shepherd, G. G., & Solheim, B. (2005). Atomic oxygen profiles (80 to 115 km) derived from wind imaging interferometer/upper atmospheric research satellite measurements of the hydroxyl and greenline airglow: Local time–latitude dependence. *Journal of Geophysical Research: Atmospheres*, *110*, D15305. https://doi.org/10.1029/2004JD005570

Sander, S. P., Abbatt, J., Barker, J. R., Burkholder, J. B., Friedl, R. R., Golden, D. M., et al. (2011). *Chemical kinetics and photochemical data for use in atmospheric studies, evaluation no. 17* (JPL Publ. 10-6). Pasadena, CA: NASA-JPL.

Scherliess, L., & Fejer, B. G. (1999). Radar and satellite global equatorial F region vertical drift model. *Journal of Geophysical Research*, *104*, 6829–6842.

Schunk, R. W., & Nagy, A. F. (2009). *Ionospheres, physics, plasma physics, and chemistry* (2nd ed., 628 pp.). Cambridge, UK: Cambridge University Press.

Sharma, R. D., Wintersteiner, P. P., & Kalogerakis, K. S. (2015). A new mechanism for OH vibrational relaxation leading to enhanced CO_2 emissions in the nocturnal mesosphere. *Geophysical Research Letters*, *42*, 4639–4647. https://doi.org/10.1002/2015GL063724

Sheese, P. E., McDade, I. C., Gattinger, R. L., & Llewellyn, E. J. (2011). Atomic oxygen densities retrieved from optical spectrograph and infrared imaging system observations of O_2 a-band airglow emission in the mesosphere and lower thermosphere. *Journal of Geophysical Research: Atmospheres*, *116*, D01303. https://doi.org/10.1029/2010JD014640

Smith, A. K., Marsh, D. R., Mlynczak, M. G., & Mast, J. C. (2010). Temporal variations of atomic oxygen in the upper mesosphere from saber. *Journal of Geophysical Research: Atmospheres*, *115*, D18309. https://doi.org/10.1029/2009JD013434

Smithtro, C. G., & Solomon, S. C. (2008). An improved parameterization of thermal electron heating by photoelectrons, with application to an x17 flare. *Journal of Geophysical Research: Space Physics*, *113*, A08307. https://doi.org/10.1029/2008JA013077

Solomon, S., Kinnison, D., Bandoro, J., & Garcia, R. (2015a). Simulation of polar ozone depletion: An update. *Journal of Geophysical Research: Atmospheres*, *120*, 7958–7974. https://doi.org/10.1002/2015JD023365

Solomon, S. C. (2017). Global modeling of thermospheric airglow in the far ultraviolet. *Journal of Geophysical Research: Space Physics*, *122*, 7834–7848. https://doi.org/10.1002/2017JA024314

Solomon, S. C., Burns, A. G., Emery, B. A., Mlynczak, M. G., Qian, L., Wang, W., et al. (2012). Modeling studies of the impact of high-speed streams and co-rotating interaction regions on the thermosphere-ionosphere. *Journal of Geophysical Research: Space Physics*, *117*, A00L11. https://doi.org/10.1029/2011JA017417

Solomon, S. C., & Qian, L. (2005). Solar extreme-ultraviolet irradiance for general circulation models. *Journal of Geophysical Research: Space Physics*, *110*, A10306. https://doi.org/10.1029/2005JA011160

Solomon, S. C., Qian, L., & Roble, R. G. (2015b). New 3-D simulations of climate change in the thermosphere. *Journal of Geophysical Research: Space Physics*, *120*, 2183–2193. https://doi.org/10.1002/2014JA020886

Swartz, W. E., & Nisbet, J. S. (1972). Revised calculations of F region ambient electron heating by photoelectrons. *Journal of Geophysical Research*, *77*, 6259–6261. https://doi.org/10.1029/JA077i031p06259

Thébault, E., Finlay, C. C., Beggan, C. D., Alken, P., Aubert, J., Barrois, O., et al. (2015). International Geomagnetic Reference Field: The 12th generation. *Earth, Planets and Space*, *67*, 79. https://doi.org/10.1186/s40623-015-0228-9

Titheridge, J. (2003). Ionisation below the night F2 layer—A global model. *Journal of Atmospheric and Solar-Terrestrial Physics*, *65*, 1035–1052. https://doi.org/10.1016/S1364-6826(03)00136-6

Wang, W. (1998). *A Thermosphere-Ionosphere Nested Grid (TING) model* (PhD dissertation, 305 pp.). Ann Arbor: The University of Michigan.

Wang, W., Lei, J., Burns, A. G., Solomon, S. C., Wiltberger, M., Xu, J., et al. (2010). Ionospheric response to the initial phase of geomagnetic storms: Common features. *Journal of Geophysical Research: Space Physics*, *115*, A07321. https://doi.org/10.1029/2009JA014461

Weimer, D. R. (2005). Improved ionospheric electrodynamic models and application to calculating joule heating rates. *Journal of Geophysical Research: Space Physics*, *110*, A05306. https://doi.org/10.1029/2004JA010884

Wu, Q., Ortland, D. A., Solomon, S. C., Skinner, W. R., & Niciejewski, R. J. (2011). Global distribution, seasonal, and inter-annual variations of mesospheric semidiurnal tide observed by TIMED TIDI. *Journal of Atmospheric and Solar-Terrestrial Physics*, *73*, 2482–2502. https://doi.org/10.1016/j.jastp.2011.08.007

Zhang, Y., & Paxton, L. (2008). An empirical kp-dependent global auroral model based on TIMED/GUVI FUV data. *Journal of Atmospheric and Solar-Terrestrial Physics*, *70*, 1231–1242. https://doi.org/10.1016/j.jastp.2008.03.008